

Fast Bayesian Functional Principal Components Analysis

Joseph Sartini ^{*1}, Xinkai Zhou¹, Liz Selvin², Scott Zeger¹, and Ciprian M. Crainiceanu¹

¹Department of Biostatistics, Johns Hopkins University

²Department of Epidemiology, Johns Hopkins University

July 11, 2025

Abstract

Functional Principal Components Analysis (FPCA) is a widely used analytic tool for dimension reduction of functional data. Traditional implementations of FPCA estimate the principal components from the data, then treat these estimates as fixed in subsequent analyses. To account for the uncertainty of PC estimates, we propose FAST, a fully-Bayesian FPCA with three core components: (1) projection of eigenfunctions onto an orthonormal spline basis; (2) efficient sampling of the orthonormal spline coefficient matrix using polar decomposition; and (3) ordering eigenvalues during sampling. Extensive simulation studies show that FAST is very stable and performs better compared to existing methods. FAST is motivated by and applied to a study of the variability in mealtime glucose from the Dietary Approaches to Stop Hypertension for Diabetes Continuous Glucose Monitoring (DASH4D CGM) study. All relevant STAN code and simulation routines are available as supplementary material.

Keywords: Bayesian Methods, Functional Data, Semiparametric Methods, Uncertainty Quantification

^{*}The DASH4D Trial is funded by a grant from the Sheikh Khalifa Stroke Institute at Johns Hopkins University School of Medicine. The DASH4D-CGM study is funded by NIH/NIDDK grant R01 DK128900. Dr. Selvin was also supported by NIH/NHLBI grant K24 HL152440. Mr. Sartini was supported by Grant Number T32 HL007024 from the NIH/NHLBI. The content is solely the responsibility of the authors and does not necessarily represent the official views of the National Institutes of Health. Abbott Diabetes Care provided continuous glucose monitoring systems for this investigator-initiated research.

1 Introduction

Functional principal component analysis (FPCA) is a common analytic approach for high-dimensional applications. FPCA approximates the covariance between all possible pairs of observations by identifying a small set of orthonormal principal components (FPCs). Using FPCs to provide a reduced-rank representation of functional data, rather than fixed (spline) bases (Rice and Wu, 2001; Shi et al., 1996), provides a data-driven representation based the leading modes of variability (James et al., 2000). While the means of estimating these FPCs can vary, e.g. polynomial smoothing (Yao et al., 2005), kernel smoothing (Staniswalis et al., 1998), or sandwich covariance smoothing (Xiao et al., 2016), the key idea remains consistent. Conditioning on the FPCs, functional models become mixed effects models with a small number of random effects and inference can be conducted using existing software (Di et al., 2009; Liu and Guo, 2012; Reiss and Ogden, 2007; Shou et al., 2015; Zhou et al., 2010). Frequentist implementations of FPCA follow a two-step approach: (1) diagonalizing a smooth estimator of the observed functional covariance; and then (2) conducting inference conditional on the FPC estimates (Crainiceanu and Goldsmith, 2010; Peng and Paul, 2009; Xiao et al., 2016). This conditional approach may lead to invalid inference in smaller samples and/or when eigenfunctions explain smaller variance (Goldsmith et al., 2013). FPC forms may be falsely identified, or FPC scores with substantial uncertainty may be used in downstream regression.

There are several Bayesian FPCA implementations which jointly model the FPCs and their scores to account for all sources of uncertainty. An early fully-Bayesian FPCA was developed by Goldsmith et al. (2015), who modeled both the fixed and random effects functions using unconstrained splines and applied post-processing to obtain orthonormal FPC samples. Jauch et al. (2021) directly sampled the FPC matrix using polar decomposition and Gaussian Process priors. In the context of sparse functional data, Ye (2024) projected the FPCs onto an orthonormal spline basis and used the Gibbs sampling approach of Hoff (2009) to sample the spline weights such that FPC orthonormality was preserved. A recent approach used variational inference based on message passing (Nolan et al., 2023).

In this paper, we introduce Fast Bayesian FPCA, or FAST for short, which integrates features of Ye (2024) and Jauch et al. (2021) along with computational optimizations to produce an MCMC approach that is stable, scalable, and extensible. FAST leverages orthogonal spline expansion to reduce the dimension of sampled FPC parameters to the corresponding weights, which are then efficiently sampled using polar decomposition. The dimensionality reduction of the posterior space by spline expansion combined with stabilizing order constraints of FPCA ensures that the approach has excellent convergence and mixing properties while being computationally efficient. All core components of FAST are easy to implement in standard Bayesian modeling software such as **STAN** (Carpenter et al., 2017) and can be extended to include covariates, multilevel, sparse, and multivariate data.

This research is motivated by the Dietary Approaches to Stop Hypertension for Diabetes Continuous Glucose Monitoring (DASH4D CGM) clinical trial. DASH4D CGM was a crossover feeding trial which included continuous glucose monitoring (CGM) during meals that were controlled and provided by the study. Participants visited the study site three times per week to provide blood samples and receive their assigned meals, all while wearing a CGM device. When participants consumed a meal at the study center, study staff recorded the start times. Here we focus on CGM data collected after the observed meals, with dysregulation of the corresponding glycemic response being known to be associated with adverse cardiovascular outcomes (Garber, 2012; Hershon et al., 2019).

Analyses of postprandial CGM glucose with verified meal times and composition are rare, and previous studies have not considered the continuous functional measurements obtained from CGM (Barua et al., 2022; Röhling et al., 2019). This paper introduces novel statistical methods designed to quantify the five-hour CGM curves from one hour before to four hours after each meal. The main results of the trial are reported elsewhere (Fang et al., 2025; Pilla et al., 2025), so this paper focuses on the variability of the CGM trajectories by diet and not on treatment effects. Specifically, it applies FPCA to the CGM curves aggregated by participant and Multilevel FPCA (MFPCA) to the individual meal response curves. The number of participants in this study is relatively small because of participant burden and data collection cost, which may result in substantial FPCA uncertainty.

The rest of the paper is organized as follows. Section 2 presents the modeling approach for FAST. Section 3 provides the STAN code. Section 4 compares FAST with existing implementations using simulation. Section 5 demonstrates the utility of FAST in estimating FPCA for the motivating data from the DASH4D clinical trial, with appropriate uncertainty quantification. Section 6 provides a short discussion.

2 Methods

2.1 FPCA model

The functional data structure has the form $Y_i(t), i = 1, \dots, N$ for $t \in \{t_1, \dots, t_M\} \in [0, 1]$, which can be thought of as latent functions observed on a finite grid. Assuming that $Y_i(t)$ are generated by the same Gaussian Process and truncating the decomposition (Karhunen, 1947; Kosambi, 1943; Loève, 1978) produces the standard FPCA model:

$$Y_i(t) = \mu(t) + \sum_{k=1}^{\infty} \xi_{ik} \phi_k(t) \approx \mu(t) + \sum_{k=1}^K \xi_{ik} \phi_k(t) + \epsilon_i(t) . \quad (1)$$

Here $\mu(t)$ is the population mean, $\phi_k(t) \in L^2([0, 1])$ for $k = 1, \dots, K$ are orthonormal eigenfunctions of the covariance operator of $Y_i(t)$, $\xi_{ik} \sim N(0, \lambda_k)$, λ_k are the eigenvalues

corresponding to $\phi_k(t)$, $\epsilon_i(t) \sim N(0, \sigma^2)$ is the error process, and $\epsilon_i(t)$ and ξ_{ik} are mutually independent over i and k .

For this paper, we fix the number of FPCs, K , which controls the rank of the smooth covariance operator. Choosing K is a difficult problem discussed extensively in the literature (Crainiceanu et al., 2024; Li et al., 2013; Yao et al., 2005). For the purpose of this paper, K is chosen based on the proportion of total variability explained. This can either be estimated using frequentist FPCA or our FAST procedure using a sequence of K s.

Model (1) is a first line approach to analysis of high dimensional data (Crainiceanu et al., 2024) because in many applications $K \ll M$ and model (1) provides a practical, low-dimensional approximation to the original high-dimensional data. Moreover, conditional on the FPCs, $\phi_k(\cdot)$, the model becomes a mixed effects model with uncorrelated random effects. In this paper we treat the eigenfunctions $\phi_k(t)$ as parameters, estimate them from the data, and account for uncertainty. *FAST provides a stable approach to simulating the posterior distribution of all parameters, including the eigenfunctions.*

2.2 Orthonormal spline expansion

All functional components are expanded using a Q -dimensional orthonormal spline basis, such that $Q \geq K$. Orthonormality is defined with respect to the scalar product on $L^2([0, 1])$, i.e. $\langle f, g \rangle = \int_0^1 f(x)g(x)dx$. Denote by $\mathbf{B}(t) = \{B_1(t), \dots, B_Q(t)\}$ the spline basis and by $\mathbf{B} \in \mathbb{R}^{M \times Q}$ the matrix representation of the spline evaluated over an M -dimensional grid. Each column of \mathbf{B} corresponds to a spline basis and each row corresponds to a sampling point. We model $\mu(t) = \mathbf{B}(t)w_\mu$ and $\phi_k(t) = \mathbf{B}(t)\psi_k$, where w_μ and ψ_k are Q -dimensional vectors of spline coefficients. In the data space, these become $\{\mu(t_1), \dots, \mu(t_M)\}^t = \mathbf{B}w_\mu$ and $\{\phi_k(t_1), \dots, \phi_k(t_M)\}^t = \mathbf{B}\psi_k$.

We will show that the $\phi_k(t)$ functions are orthonormal if and only if $\Psi^t \Psi = I_{K \times K}$, where $\Psi = [\psi_1 | \dots | \psi_K]$ is the $Q \times K$ dimensional matrix obtained by column binding the ψ_k . Indeed, as $\mathbf{B}(t)$ is an orthonormal spline basis, $\langle B_i(t), B_j(t) \rangle = 1$ if $i = j$ and 0 otherwise. Therefore, $\langle \phi_k(t), \phi_{k'}(t) \rangle$ is equal to

$$\int_0^1 [\mathbf{B}(t)\psi_k][\mathbf{B}(t)\psi_{k'}]dt = \sum_{i=1}^Q \sum_{j=1}^Q \psi_{k,i} \psi_{k',j} \left[\int_0^1 B_i(t) B_j(t) dt \right] = \psi_k^t \psi_{k'}.$$

The quantity $\psi_k^t \psi_{k'} = 1$ when $k = k'$ and 0 if and only if Ψ matrix is orthonormal. Therefore, the eigenfunctions $\phi_k(t)$ are orthonormal in $L^2([0, 1])$ if and only if the low-dimensional spline coefficients are orthonormal in \mathbb{R}^Q . This is a crucial point of our methodology, as the orthonormality of the eigenfunctions (in infinite or high dimensional spaces) is controlled by orthonormality of vectors in a small dimensional space. Because it is much easier the sample from a small dimensional space, this projection is one of the main reasons the FAST

method is stable and computationally efficient.

In functional data analysis, orthonormality in the theoretical $L^2([0, 1])$ functional space is often confounded with orthonormality in the \mathbb{R}^M observed vector space. For a fixed M , the difference is minimal, as this corresponds to approximating the functional inner product with the corresponding Riemann sum – the inner product in \mathbb{R}^M scaled by $1/M$. However, when the dimension is changed from M_1 to M_2 , the vector inner product must be adjusted by $\sqrt{M_1/M_2}$, whereas the functional inner product is not affected. FAST can be used in the vector space as well by choosing matrix \mathbf{B} such that $\mathbf{B}^t \mathbf{B} = \mathbf{I}_Q$. The resulting FPC matrix $\mathbf{B}\Psi$ is then a product of orthonormal matrices. To maintain robustness to different M , we focus here on the functional orthonormality. However, the software implementation in supplementary materials can leverage vector orthormality, as well.

The basis dimension Q must be sufficiently large to capture the maximum complexity of the subject-specific functions. We follow here the standard recommendations for penalized splines and use $Q \in [20, 40]$ (Ruppert, 2002), which performed well in our tests (see Supplement Sections S4.2). The choice of the basis matrix \mathbf{B} can substantially impact the computational stability and efficiency of FAST. While, in theory, any spline matrix \mathbf{B} which is orthonormal in $L^2[0, 1]$ could be used, in practice some approaches have better computational properties and interpretation properties. We choose as our basis ‘Splinets’, an orthonormalized B-spline basis designed by Liu et al. (2020) to maintain temporal localization. We augment their basis with a slope and intercept, appropriately orthonormalized.

2.3 Priors

We add smoothing priors for both $\mu(t)$ and the FPCs $\phi_k(t)$ using penalties of the type $\alpha \int f^2(t)dt + (1 - \alpha) \int \{f''(t)\}^2 dt$, where $f(\cdot)$ denotes a generic function. This penalty, used by Goldsmith et al. (2015), contains the fixed weighting parameter α , where $\alpha = 0$ corresponds to the famous penalized spline prior (Craven and Wahba, 1979; O’Sullivan, 1986). If $f(t) = \mathbf{B}(t)\theta$, then the penalty is a quadratic form of θ with associated matrix \mathbf{P}_α . Supplement Section S1 covers derivation of \mathbf{P}_α . We use $\alpha = 0.1$ for consistency with existing implementations, but FAST can handle any $\alpha \in [0, 1]$. Supplement Section S4.3 indicates robustness to reasonable choice of α . The quadratic penalties are equivalent to Normal priors when \mathbf{P}_α is non-degenerate (Brumback et al., 1999; Ruppert et al., 2003; Wood, 2006). These penalties/prior distributions $f(w_\mu), f(\psi_k)$ have the following forms:

$$f(w_\mu) \propto h_\mu^{R(\mathbf{P}_\alpha)/2} \exp \left\{ -\frac{h_\mu}{2} w_\mu^t \mathbf{P}_\alpha w_\mu \right\}, \quad f(\psi_k) \propto h_k^{R(\mathbf{P}_\alpha)/2} \exp \left\{ -\frac{h_k}{2} \psi_k^t \mathbf{P}_\alpha \psi_k \right\},$$

where $\text{rank } \mathbf{P}_\alpha$ is the rank of the matrix \mathbf{P}_α and $h_\mu, h_k > 0$ are the smoothing parameters for $\mu(\cdot)$ and $\phi(\cdot)$, respectively. FAST uses separate parameters for each functional component, in-line with Ye (2024) and Goldsmith et al. (2015).

We assume that the inverse variance components, including the smoothing parameters, have non-informative Gamma priors with the shape and rate equal to 0.001. For discussion on the choice of Gamma priors for inverse variance components, see Crainiceanu et al. (2005); Crainiceanu and Goldsmith (2010)

2.4 Polar decomposition

With these priors, the conditional posterior distributions for all parameters except Ψ have analytical forms; see Supplement Section S2. The $Q \times K$ dimensional matrix parameter Ψ is an element in the space of orthonormal matrices. This space is called the Stiefel manifold (James, 1976), has a finite volume, and is denoted as $\mathcal{V}_{K,Q}$ (Chikuse, 2003). We assume a uniform prior for Ψ over $\mathcal{V}_{K,Q}$, with density $\mathbb{1}(\Psi \in \mathcal{V}_{K,Q})$ (Mardia and Khatri, 1977).

Result 1. *The conditional posterior distribution of the eigenfunction matrix Ψ is:*

$$f(\Psi | \text{others}) \propto \text{etr} \left[\frac{\Xi(\mathbf{Y} - \mathbf{1}_N^t \otimes \mathbf{B}w_\mu)^t \mathbf{B} \Psi}{\sigma^2} - \frac{\Xi \Xi^t \Psi^t \mathbf{B}^t \mathbf{B} \Psi}{2\sigma^2} - \frac{\mathbf{H} \Psi^t \mathbf{P} \Psi}{2} \right] \mathbb{1}(\Psi \in \mathcal{V}_{K,Q}),$$

where $\mathbf{H} = \text{diag}(h_1, \dots, h_K)$, Ξ is a $N \times K$ dimensional matrix with the (i, k) entry equal to $\xi_{i,k}$, and the matrix \mathbf{Y} is the $N \times M$ dimensional matrix with the row i equal to Y_i^t . The quantity $\mathbf{1}_N$ is the N -dimensional column vector of ones, the symbol \otimes denotes the Kronecker product of matrices, and ‘‘etr’’ denotes the exponential of the matrix trace.

The distribution in Result 1 does not follow a known form, though it is close to the generalized Langevin-Bingham family (Hoff, 2009). We sample this distribution indirectly using the polar decomposition of matrices. The polar decomposition of the $Q \times K$ dimensional matrix \mathbf{X} is $\mathbf{X} = \mathbf{U}\mathbf{P}$, where $\mathbf{U} \in \mathbb{R}^{Q \times K}$ is orthonormal (on the Stiefel manifold $\mathcal{V}_{K,Q}$) and $\mathbf{P} \in \mathbb{R}^{K \times K}$ is positive semi-definite. The polar decomposition is unique when \mathbf{X} is full rank K . Crucially, if \mathbf{X} has independent $N(0, 1)$ entries, then the matrix \mathbf{U} is uniformly distributed over the Stiefel manifold $\mathcal{V}_{K,Q}$ (Chikuse, 2003). Therefore, the matrix Ψ can be sampled indirectly by imposing independent, entry-wise $N(0, 1)$ priors on \mathbf{X} , corresponding to a uniform prior density on $\mathcal{V}_{K,Q}$. This is a particular case of the parameter expansion strategy used by Jauch et al. (2021); Meng and Bouchard (2024); Park (2025).

FAST performs polar decomposition using the eigendecomposition $\mathbf{X}^t \mathbf{X} = \mathbf{Z} \mathbf{D} \mathbf{Z}^t$, defining $\Psi = \mathbf{X} \mathbf{Z} \mathbf{D}^{-1/2} \mathbf{Z}^t$ and $\mathbf{P} = \Psi^t \mathbf{X}$. It can be easily verified that $\Psi^t \Psi = I_Q$. Using this decomposition to sample Ψ works well because: (1) the element-wise independent $N(0, 1)$ priors on \mathbf{X} are computationally simple; (2) the matrix $\mathbf{X} \in \mathbb{R}^{Q \times K}$ is much smaller dimensional than matrix of eigenfunctions $\Phi \in \mathbb{R}^{M \times K}$ when $Q \ll M$; and (3) deterministically calculating Φ from \mathbf{X} can be accomplished efficiently using standard linear algebra routines.

2.5 Alignment, Estimation, and Convergence

There are two main sources of non-identifiability for the eigenfunctions and scores in FPCA: sign flipping and ordering. This problem is exacerbated by the complex geometry of the Stiefel manifold. To address these issues, FAST incorporates both constrained MCMC sampling and post-processing steps. During sampling, strict ordering of the λ_k is imposed. In post-processing, we first re-order FPCs/scores according to the score sample variances, then align the signs to maximize vector correlation between each $\phi_k(\cdot)$ sample and the corresponding first FPC sample after burn-in. This approach is different from existing Bayesian implementations (Goldsmith et al., 2015; Jauch et al., 2021), but it is computationally simple and performed well in our testing.

An additional problem is that the point-wise means of the FPC samples are not guaranteed to be orthonormal. To address that, we take the element-wise mean of the spline coefficient Ψ matrix and orthonormalize the results. The resulting $\widehat{\Psi}$ will be orthonormal, and thus produce orthonormal FPC estimate $\widehat{\Phi} = \mathbf{B}\widehat{\Psi}$ as described in Section 2.2.

To monitor convergence of FAST we use the Gelman-Rubin RHat statistic for all model parameters (Gelman and Rubin, 1992), including the FPCs. This is done after post-processing the PCs and scores.

2.6 Extensions

FAST can be extended to multilevel, structural, and longitudinal functional data (Di et al., 2009; Greven et al., 2010; Shou et al., 2015), which are becoming increasingly common in applications. We demonstrate how to extend FAST to fit a multilevel model. The data structure is of the form $Y_{ij}(t), i = 1, \dots, N, j = 1, \dots, J_i, t \in T = \{t_1, \dots, t_M\}$, where there are J_i observations for each group i . A model for such data is MFPCA (Di et al., 2009; Zipunnikov et al., 2011)

$$Y_{ij}(t) = \mu(t) + \eta_j(t) + \sum_{k=1}^{K_1} \xi_{ik} \phi_k^{(1)}(t) + \sum_{l=1}^{K_2} \zeta_{ijl} \phi_l^{(2)}(t) + \epsilon_{ij}(t), \quad (2)$$

where $\mu(t)$ is the population mean and $\eta_j(t)$ are visit-specific deviations from the population mean. The subject-level (level 1) deviations from the visit-specific mean are modeled by $U_i(t) = \sum_{k=1}^{K_1} \xi_{ik} \phi_k^{(1)}(t)$, where $\phi_k^{(1)}(t)$, $k = 1, \dots, K_1$ are the first level eigenfunctions, $\xi_{ik} \sim N(0, \lambda_k^{(1)})$, and $\lambda_k^{(1)}$ are the eigenvalues corresponding to $\phi_k^{(1)}(t)$. The subject/visit-specific (level 2) deviations from the subject-specific mean are modeled by $W_{ij}(t) = \sum_{l=1}^{K_2} \zeta_{ijl} \phi_l^{(2)}(t)$, where $\phi_l^{(2)}(t)$, $l = 1, \dots, K_2$ are the second level eigenfunctions, $\zeta_{ijl} \sim N(0, \lambda_l^{(2)})$, and $\lambda_l^{(2)}$ are the eigenvalues corresponding to $\phi_l^{(2)}(t)$. Finally, $\epsilon_{ij}(t) \sim N(0, \sigma^2)$ is the error process. All functional components, $\epsilon_{ij}(t)$, $U_i(t)$ and $W_{ij}(t)$, are assumed to be mutually independent.

The fixed effects, population mean $\mu(t)$ and the visit-specific deviations $\eta_j(t)$, are mod-

eled using any penalized splines. The subject-specific $U_i(t) = \sum_{k=1}^{K_1} \xi_{ik} \phi_k^{(1)}(t)$ and the visit-specific $W_{ij}(t) = \sum_{l=1}^{K_2} \zeta_{ijl} \phi_l^{(2)}(t)$ can be modeled separately using the same techniques described in Sections 2.2, 2.4, and 2.5. This is the first Bayesian MFPCA implementation directly modeling the FPCs.

3 Bayesian implementation in STAN

In this section, we provide the simple STAN Carpenter et al. (2017) implementation of FAST. We begin with the `data` section, which declares constants and imports the data, spline basis, and penalty matrix. All notation is as used in Section 2.

```
data{
  int N; // Number of time series
  int M; // Number of observations
  int Q; // Number of spline bases
  int K; // Number of Eigenfunctions

  matrix[N, M] Y; // Functional data
  matrix[M, Q] B; // Orthogonal spline basis
  matrix[Q, Q] P; // Penalty matrix for splines
}
```

In the `parameters` block, we model the matrix \mathbf{X} (\mathbf{X}) rather than Ψ , which is obtained from \mathbf{X} via polar decomposition. This block also contains the eigenvalues λ_k (`lambda`) stored using a `positive_ordered` type, ordering the eigenvalues and corresponding eigenfunctions. The matrix `Scores` is the $N \times K$ score matrix Ξ introduced in Result 1.

```
parameters{
  real<lower=0> sigma2; // Error in observation

  // Mean structure
  vector[Q] w_mu; // Population mean parameters
  real<lower=0> h_mu; // Population mean smoothing parameter

  // Covariance structure
  positive_ordered[K] lambda; // Eigenvalues
  vector<lower=0>[K] H; // EF smoothing parameters
  matrix[Q, K] X; // Unconstrained EF weights (X)
  matrix[N, K] Scores; // EF scores (xi)
}
```

The `transformed parameters` section contains deterministic functions of the data and model parameters. The key component of this block is the calculation of Ψ (`Psi`) as the orthogonal component of the polar decomposition $\mathbf{X} = \Psi \mathbf{P}$. More precisely, $\Psi = \mathbf{X} \mathbf{Z} \mathbf{D}^{-1/2} \mathbf{Z}^t$, where \mathbf{Z} (`exec_XtX`) is the $K \times K$ dimensional matrix of eigenvectors of $\mathbf{X}^t \mathbf{X}$ and \mathbf{D} (`diag(eval_XtX)`) is a diagonal matrix containing the corresponding K eigenvalues.

Because $\mathbf{X} \in \mathbb{R}^{Q \times K}$ is low dimensional, all these operations are efficient.

```
// Calculate observed parameters from latent
transformed parameters{
    // Population mean
    vector[M] mu = (B * w_mu)';
    // Polar decomposition
    matrix[Q,K] Psi;
    {
        matrix[K,K] evec_XtX = eigenvectors_sym(X'*X);
        vector[K] eval_XtX = eigenvalues_sym(X'*X);
        Psi = X*evec_XtX*diag_matrix(1/sqrt(eval_XtX))*evec_XtX';
    }
}
```

The model proceeds with the specification of priors within the `model` section. The key component is the prior on Ψ (`Psi`), which just requires specifying independent $N(0, 1)$ priors for each entry of the matrix \mathbf{X} (`X`). Combined with the polar decomposition in the `transformed parameters` block, this induces a uniform prior on Ψ over the Stiefel manifold, $\mathcal{V}_{K,Q}$. FAST thus models the FPCs through the small-dimensional $\mathbf{X} \in \mathbb{R}^{Q \times K}$, constrained by the size of the spline basis and number of FPCs. This dimensionality reduction likely contributes to the much improved computational efficiency. All other priors are as described in Section 2.3.

```
model{
    // (Inverse) variance priors
    H ~ gamma(0.001, 0.001);
    h_mu ~ gamma(0.001, 0.001);
    lambda ~ inv_gamma(0.001, 0.001);
    sigma2 ~ inv_gamma(0.001, 0.001);

    // Smoothing additions to the target density
    target += Q/2.0 * log(h_mu) - h_mu / 2.0 * w_mu' * P * w_mu;
    for(i in 1:K){
        target += Q/2.0 * log(H[i]) - H[i] / 2.0 * Psi[,i]' * P * Psi[,i];
    }

    // Indirect uniform prior on Stiefel manifold
    to_vector(X) ~ normal(0,1);

    // FPCA-based Score priors
    for(i in 1:K){
        to_vector(Scores[,k]) ~ normal(0, sqrt(lambda[k]));
    }
    :
}
```

We next present the likelihood contribution. This portion of the `model` block computes

the random deviations $\theta_i(t) = \sum_{k=1}^K \xi_{ik} \phi_k(t) = \sum_{k=1}^K \xi_{ik} \{\mathbf{B}(t) \psi_k\}$. If Θ (Theta) is the $N \times M$ dimensional matrix with (i, m) entry equal to $\theta_i(t_m)$, it can be shown that $\Theta = \Xi(\mathbf{B}\Psi)^t$. This value is computed, used, and discarded to conserve memory. The model finally incorporates the observed data contribution, following the FPCA data likelihood in Section 2.1, using a vectorized distributional statement for computational efficiency.

```
model{
  :
  { // Data Likelihood
    matrix[N,M] Theta = Scores * (B * Psi)';
    to_vector(Y) ~ normal(to_vector(rep_matrix(mu, N) + Theta), sqrt(sigma2));
  }
}
```

This implementation suggests how to extend FAST to more complex structures. For MFPCA, we sample two spline coefficient matrices Ψ_1 and Ψ_2 . For each matrix, we independently model a latent matrix: \mathbf{X}_1 for Ψ_1 and \mathbf{X}_2 for Ψ_2 . We assign independent $N(0, 1)$ priors to the entries of both \mathbf{X}_1 and \mathbf{X}_2 . The Ψ_1 and Ψ_2 matrices are obtained via separate polar decompositions in `transformed parameters`. All other implementation components are straightforward, just requiring careful accounting of indices. We present both the implementation and simulation evaluation in Supplement Section S3.4.

4 Simulations

We consider the following two simulation scenarios for model (1), where $f_k(t)$ are the Legendre polynomials on $[0, 1]$:

(S1) Emulation of CGM data from Section 5

$$\begin{aligned}\mu(t) &= 140 - 20 \times f_2(t), \sigma^2 = 4, \lambda_k = \{2250, 450, 150\} \\ \phi_k(t) &= \{f_0(t), \sqrt{\frac{84}{31}}[f_1(t) - 0.5f_3(t)], -\sqrt{5}f_2(t)\}\end{aligned}$$

(S2) Canonical FPCA example from Xiao et al. (2016)

$$\begin{aligned}\mu(t) &= 0, \sigma^2 = 0.35, \lambda_k = \{1, 0.5, 0.25\} \\ \phi_k(t) &= \{\sqrt{2} \sin(2\pi t), \sqrt{2} \cos(4\pi t), \sqrt{2} \sin(4\pi t)\}\end{aligned}$$

For each scenario we generate 200 datasets with $N = 50$ functions observed at $M = 50$ points distributed along $[0, 1]$ according to quadrature. FAST is compared to the Generalized Function-on-Scalar Regression of Goldsmith et al. (2015) (labeled “GFSR”), polar expansion in the observed data space from Jauch et al. (2021) (labeled “POLAR”), and Variational Message Passing from Nolan et al. (2023) (labeled “VMP”). We do not compare with Ye (2024) due to there being no available software. For the MCMC-based approaches, we performed 1500 sampling iterations and discarded the first 1000 as burn-in. This was chosen based upon the convergence properties of FAST and kept uniform between methods.

To obtain the orthonormal FPCs from the unconstrained samples of GFSR, we leverage the orthogonalization procedure suggested by Goldsmith et al. (2015). This involves calculating the SVD of the unconstrained FPC matrix sample and taking the right singular vectors. The scores are correspondingly transformed by the left singular vectors and diagonal matrix of singular values.

As FAST, POLAR, and GFSR all have the same identifiability issues described in Section 2.5, we applied the post-processing steps described in that section to these three methods. FPC/score signs were then aligned with those of the true underlying FPCs for the purposes of evaluation. Similar to FAST, both POLAR and GFSR require procedures to produce orthonormal (in the vector sense) FPC estimates. For POLAR, Jauch et al. (2021) recommends taking the right singular vectors of the mean smoothed data. As for GFSR, we take the point-wise mean of the non-orthogonal latent principal component matrix, then apply the SVD-based rotation Goldsmith et al. (2015) describes. VMP does not provide explicit samples, just FPC estimates.

POLAR, GFSR, and VMP all produce FPC estimates/samples which are orthonormal in the vector sense. So, we rescale the FPC estimates for these methods to have norm 1 in $L^2([0, 1])$, estimated using Gaussian quadrature weights.

We first focus on the Integrated Square Error (ISE) for FPCs $\phi_k(t)$. If $\widehat{\phi}_k^b(t)$ is the posterior estimate of $\phi_k(t)$ for simulated data set $b \in \{1, \dots, B\}$, ISE is defined as:

$$\text{ISE}^b\{\phi_k(\cdot)\} = \int_0^1 \{\widehat{\phi}_k^b(t) - \phi_k(t)\}^2 dt \approx \sum_{m=1}^M w(t_m) \{\widehat{\phi}_k^b(t_m) - \phi_k(t_m)\}^2,$$

where $w(\cdot)$ are the corresponding Gaussian quadrature weights at t_m , $m = 1, \dots, M$. Combining the ISE^b values over simulations provides a B -dimensional vectors for each method and each principal component. Figure 1 displays the boxplots of these ISE by principal component (column) for scenario S1 (first row) and scenario S2 (second row) and method. Results indicate that FAST consistently outperforms existing methods.

We also estimate pointwise posterior coverage probabilities of the true FPCs $\phi_k(t)$, $k = 1, \dots, K$. For each simulated data set $b \in \{1, \dots, B\}$, we obtain the equal-tail 95% credible intervals at the observed time points t_m , $m = 1, \dots, M$. The proportion of times these credible intervals cover the true function is calculated over the t_m for each combination of b and k . These proportions are then collected in a vector of length $B = 200$ for each function $\phi_k(t)$. VMP does not produce credible intervals for the FPCs, so it is excluded from this comparison.

Figure 2 displays the kernel smooth of the estimated point-wise coverage proportions for FAST, POLAR, and GFSR using the same structure as Figure 1. FAST performs well in all scenarios, consistently out-performing the other approaches.

Figures 1 and 2 indicate that FAST has an advantage in all scenarios, but the advantage is particularly striking for $\phi_3(t)$ in S1. In this case, the mean can be written as a linear

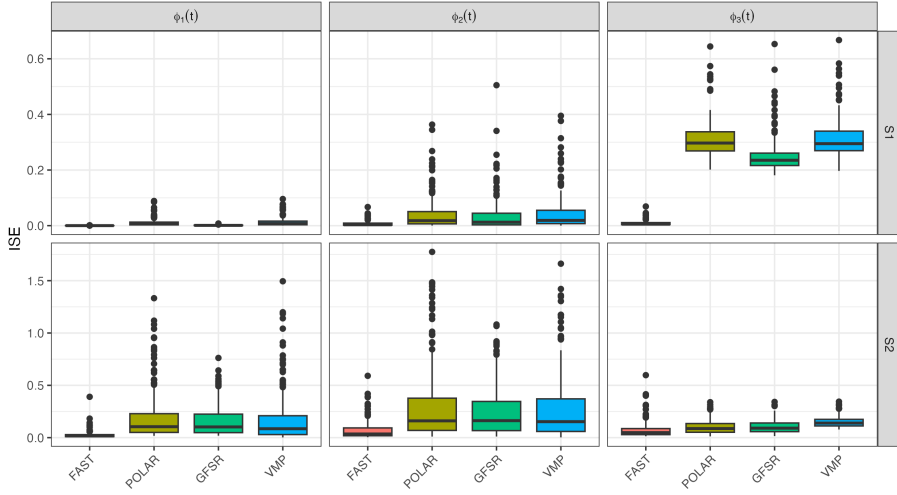


Figure 1: ISE Boxplots for FAST, POLAR, GFSR, and VMP. Row indicates simulation scenario, S1 then S2. Each column corresponds to a particular eigenfunction.

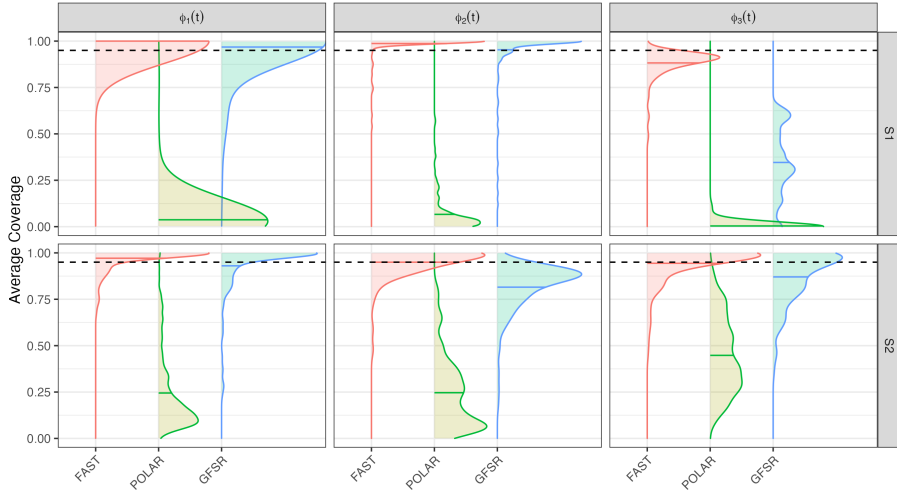


Figure 2: Kernel smoother of 95% credible interval coverage probabilities of the true FPCs for FAST, POLAR, and GFSR. Row indicates simulation scenario, S1 then S2. Each column corresponds to a particular eigenfunction. Distribution means: horizontal solid lines; nominal 95% level: horizontal dotted lines.

combination of $\phi_1(t)$ and $\phi_3(t)$: $\mu(t) = 140\phi_1(t) + 4\sqrt{5}\phi_3(t)$. This choice makes the problem more challenging in finite samples, when information may leak between the mean and covariance; see, example, Zhou et al. (2025) for a more detailed discussion.

For inference on the mean, $\mu(t)$, we only compared to GFSR, as neither the VMP nor POLAR perform inference on this component. Results indicate that FAST produces smaller ISE and better coverage probability; see Supplement Section S3.2 for more details.

We also compared estimation accuracy and posterior coverage of credible intervals for the scores ξ_k . Accuracy is calculated as mean square error aggregated by FPC, k , within

each simulation, b . Coverage was calculated as the proportion of times the equal-tail 95% credible intervals cover the corresponding true scores; see results in Supplement Section S3.3. FAST outperforms the other methods and has near nominal coverage.

Table 1 provides computation times in minutes on a personal laptop (MacBook Pro, 3.49 GHz and 32GB RAM) as both N (number of subjects) and M (number of observation points) scale up for scenario S1. The left column provides times for $N = 50$ and $M \in \{50, 100, 250, 500\}$, while the right provides times for $M = 50$ and $N \in \{50, 100, 250, 500\}$.

Fixed $N = 50$					Fixed $M = 50$				
M	FAST	GFSR	POLAR	VMP	N	FAST	GFSR	POLAR	VMP
50	2.9	24.3	9.2	0.2	50	2.9	24.3	9.2	0.2
100	5.9	39.5	28.5	1.0	100	3.5	43.2	15.4	0.6
250	13.0	82.8	—	1.2	250	5.8	47.2	29.0	0.6
500	37.3	151.0	—	5.2	500	14.4	27.8	52.1	0.7

Table 1: Computation times (in minutes) for each combination of scale and method (simulation S1). All methods evaluated on the same simulated dataset for each N, M combination.

FAST and GFSR scale approximately linearly with M , though GFSR has a substantially higher slope. For N , FAST and POLAR scale linearly, while GFSR seems to be more performant with higher N , possibly due to the increased information better specifying the posterior geometry. We could not fit POLAR for $M \geq 250$ because it uses too much memory. VMP is the fastest, not unexpected given the approximation inherent to the technique. All MCMC-based methods were run for 1500 iterations with the first 1000 discarded as burn-in; however, the convergence characteristics were not uniform. FAST and POLAR exhibit lower RHats (≤ 1.05) compared to GFSR (≤ 1.25), which may need more warm-up. The computation time of FAST is relatively robust to different Q and K values, so long as the chosen K was at least the true value (see Supplement Section S4.4).

Simulations for the multilevel scenario provide similar results; see Supplement Section S3.4. POLAR was not included because it does not have a multilevel implementation.

5 Data analysis: The DASH4D CGM Study

Dietary Approaches to Stop Hypertension for Diabetes (DASH4D, NCT04286555) is a nutritional trial designed to assess how blood pressure and glucose respond to combinations of DASH-style and low-sodium diets in persons with type 2 diabetes (T2D). The study team prepared four diets: DASH4D diet with lower sodium, DASH4D diet with higher sodium, Comparison diet with lower sodium, and Comparison diet with higher sodium. Weight was held constant by adjusting calorie level. Diet effects were observed through a single-site, 4-period crossover design (Pilla et al., 2025). Each period consisted of 5 weeks of feeding a diet followed by a ≥ 1 -week break (median 2 weeks). There were $N = 105$ randomized

T2D participants recruited from the Baltimore area, of which $N = 65$ had meal timing data. Participants with meal timing data had a median age of 68 years, were 66% female, and had the following race distribution: 6.2% Asian, 87.7% Black, and 6.2% White.

The DASH4D CGM sub-study was conducted to evaluate the impact of the dietary intervention on glucose assessed by CGM. Participants wore the Abbott Freestyle Libre Pro (Abbott Diabetes Care), placed near the middle of the third week and worn into the fifth week for each feeding period. The CGM devices were placed on the back of the upper arm (approved location) by trained technicians. These devices record interstitial glucose every 15 minutes. The Libre Pro is a masked CGM system, so participants were not aware of the glucose measurements (Wang et al., 2025).

5.1 Mealtimes CGM glucose

During feeding periods, participants ate meals at the study site 3 days each week. Clinic staff observed consenting participants to document meal timing. We used these timestamps to extract CGM data starting 1 hour before and ending 4 hours after each meal began. There were ≤ 20 such 5-hour periods per participant. The final dataset comprised 768 meals over 65 individuals. This data is not yet available as trial results are forthcoming.

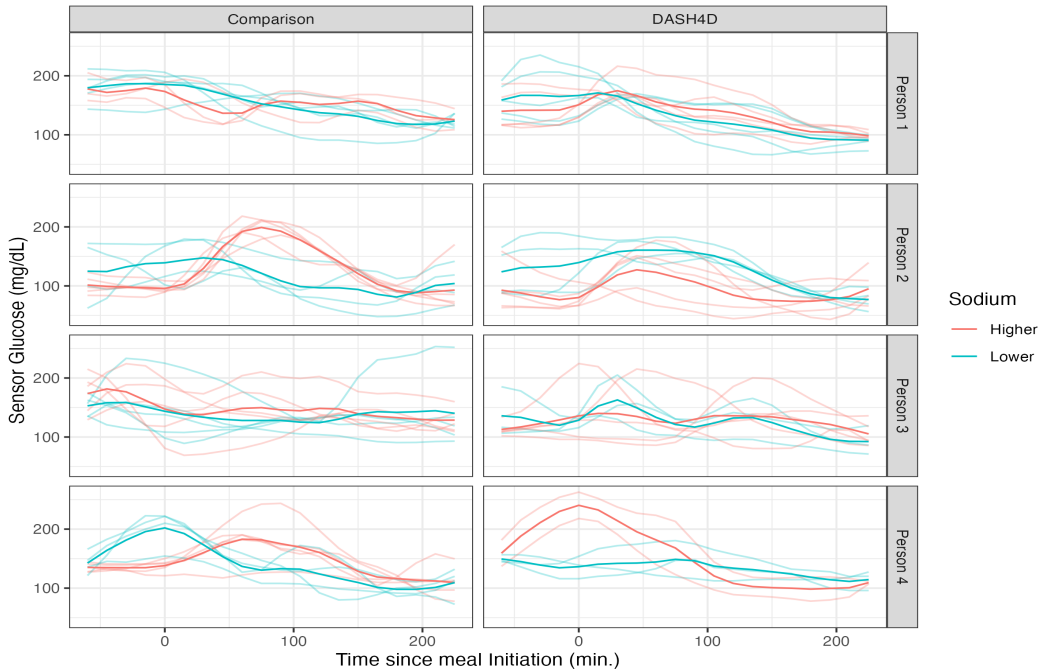


Figure 3: Mealtime CGM for 4 participants (one per row), for the Comparison (left column) and DASH4D (right column) diets. Sodium level within diet type is indicated by color. X-axis: time from meal initiation, y-axis: CGM in mg/dL. Person- and diet-specific average curves are darker, while meal-specific curves are lighter.

Figure 3 provides a visualization of mealtime CGM for four randomly-sampled study

participants. The x-axis in each panel corresponds to time in minutes from meal initiation; the y-axis is the recorded glucose. Each row corresponds to a participant. The first column is for Comparison meals, and the second is for DASH4D meals. Curve color corresponds to sodium level, and darker curves are within-person averages. Given this data structure, one could model the average average curves within person using a single-level FPCA or the meal-specific trajectories using a two-level FPCA to capture both the participant-specific averages (level 1) and the meal-specific deviations (level 2) within each diet. We undertake these analyses in Sections 5.2 and 5.3, respectively.

5.2 Bayesian FPCA of average CGM within diets

We fit FAST to the participant average CGM curves for each diet separately (darker curves in Figure 3) using a spline basis of dimension $Q = 20$ and $K = 3$ FPCs. This number of FPCs explained $\geq 95\%$ of the variability across diets (see Supplemental Figure S15) The number of curves per-diet ranges between 36 and 49, so accounting for variability in FPC estimates is of particular importance (Goldsmith et al., 2013).

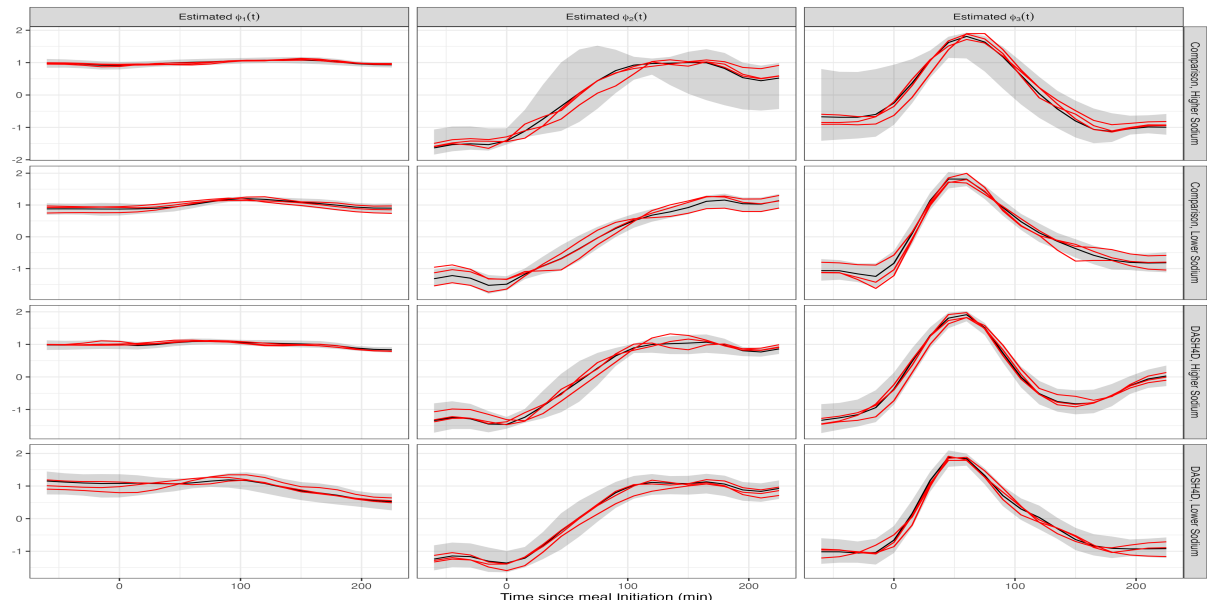


Figure 4: Bayesian FPCA results for the first three FPCs (columns) for each of the four diets (rows). X-axis: time relative to meal initiation. Black curves: posterior mean; red curves: three FPC posterior samples; shaded areas: point-wise 95% credible intervals.

Figure 4 displays results for Bayesian FPCA inference for the first three PCs (columns) for the four diets (rows). For all panels the x-axis is the time from the start of the meal, the black curves are the posterior means, the red curves are three samples from the posterior of the PCs, and the shaded areas are point-wise, equal-tail 95% credible intervals. The red curves correspond to the same sample iterations across PCs.

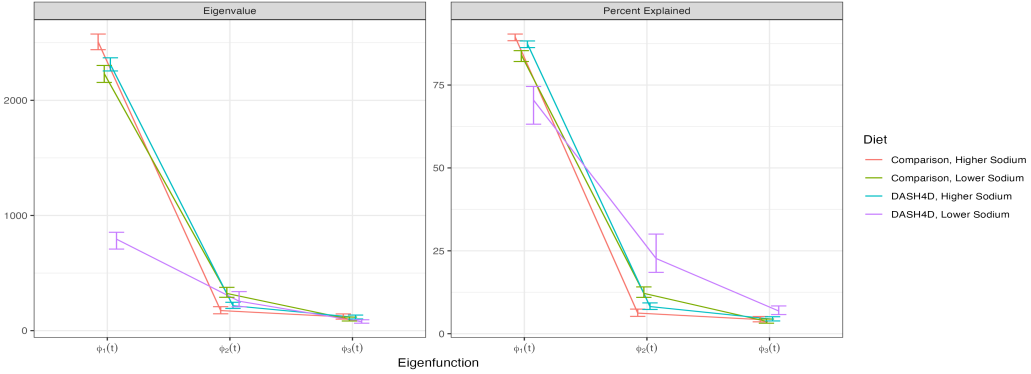


Figure 5: Eigenvalues (left panel) and percent-variability (right panel) estimates and 95% credible intervals for each of the four diets (one color corresponds to one diet).

Figure 5 provides the eigenvalues (left panel) and percent variance explained (right panel) for the eigenfunctions displayed in Figure 4. Diet is indicated by color.

Posterior eigenfunction estimates $\hat{\phi}_k(t)$ are qualitatively similar across diets in Figure 4. The primary modes of variability $\hat{\phi}_1(t)$ are nearly constant with a small curvature. Higher scores on these components correspond to higher CGM responses over the entire mealtime period. The sample-to-sample variability in the shape of $\phi_1(t)$ is low. Moreover, $\phi_1(t)$ explains 75 to 85% of the observed variability. This quantifies the importance of the mean postprandial glucose level (Garber, 2012). The second FPCs, $\hat{\phi}_2(t)$, generally exhibit an *S* pattern. Therefore, individuals with a higher positive score on $\hat{\phi}_2(t)$ have lower glucose in the pre-prandial and immediate postprandial period with a larger response one to four hours after eating. The third FPCs, $\hat{\phi}_3(t)$, are negative during the hour before the meal, increase to a peak positive value about 50 to 70 minutes after food intake, and decrease back to negative values about 150 – 200 minutes after the meal. Therefore, individuals with higher scores on $\hat{\phi}_3(t)$ tend to have a to lower glucose before the meal and a rapid glucose increase after the meal. Sample-to-sample variability of both the $\phi_2(t)$ and $\phi_3(t)$ is higher than that of $\phi_1(t)$, likely due to the smaller signal.

The variability of glucose response in the DASH4D/lower sodium diet is much lower than for the other three diets. Figure 5 indicates that $\hat{\lambda}_1(t)$ is ≈ 3 times smaller for this diet compared to the others. This diet, the primary interest to the DASH4D study, appears to be associated with a more stable glycemic response between participants.

FAST produces reasonable results, qualitatively consistent with standard FPCA, across all four diets. Each model takes 20 – 45 seconds (depending on the diet) to fit on a personal laptop using 5000 iterations with the first 2500 discarded as burn-in. We employ the routine from Section 2.5 to assess convergence of the scores, ξ_{ik} , and sampled points along the domain for each FPC, $\phi_k(t_m)$. Final Gelman-Rubin statistics were ≤ 1.01 . Despite differences in sampling frequency per participant, results were similar when fitting FPCA to randomly sampled meals; see Supplement Section S5.2.

5.3 Bayesian MFPCA of individual CGM curves

So far, we have ignored the variability of meal-specific CGM curves around the subject-specific mean. This could raise questions about accounting for all observed variability, different number of meals per person, and representativeness of the average curves. To address these problems, we fit the multilevel extension of FAST described in Section 2.6 for each diet separately, with meals nested within participants. We use a rich spline basis of dimension $Q = 20$, $K_1 = 2$ FPCs at the subject level, and $K_2 = 3$ FPCs at the meal level. These choices explain $\geq 80\%$ variability at both levels. The number of observed meals ranges from 147 to 219 for each diet, with at most five meals per participant. There is no reason to assume that meal/visit order has effect, so we set $\eta_j(t) = 0$ for all j .

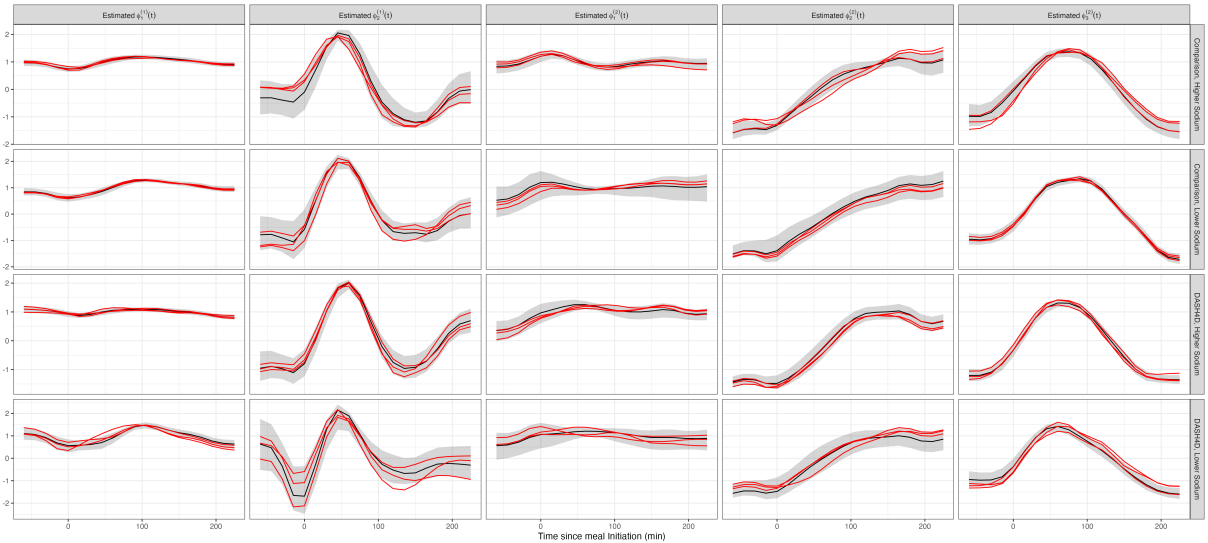


Figure 6: Bayesian MFPCA results for the first two PCs at the subject level and first three PCs at the meal level. Each column corresponds to an FPC and each row corresponds to a diet. X-axis: time from the meal start. Plotting conventions are consistent with Figure 4.

Figure 6 displays the Bayesian MFPCA results, with row indicating diet and column indicating FPC. The first two columns correspond to the subject level, while the last three correspond to the meal level. Plotting conventions are consistent with those in Figure 4.

Figure 7 provides the estimated variability (left panels) and percent variability explained (right panels) within level and diet. The first row of panels corresponds to the subject (level 1) while the second row of panels corresponds to the meal (level 2). Each color corresponds to a diet. As in the single level analyses, Figure 6 indicates qualitative similarity of estimates $\hat{\phi}_k^{(1)}(t), \hat{\phi}_l^{(2)}(t)$ across diets. The primary mode of variability within each diet is $\hat{\phi}_1^{(1)}(t)$, a nearly constant function. Higher subject scores on this component correspond to higher subject-specific glucose over the entire observation window. The sample-to-sample variability in the shape of $\hat{\phi}_1^{(1)}(t)$ is consistently low, indicating confidence in this functional form. There is some heterogeneity in the percent variability explained by this component,

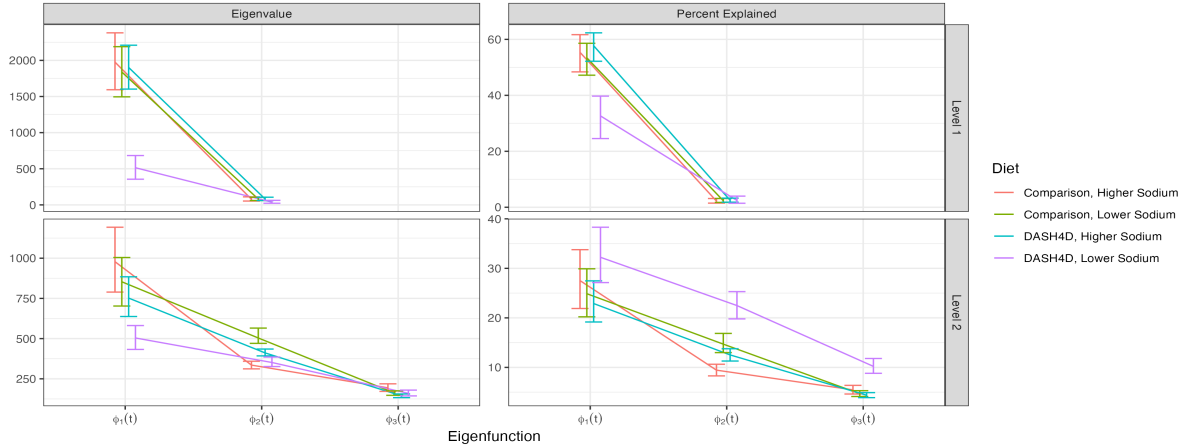


Figure 7: Eigenvalues (left panels), percent-variability explained (right panels) within level (first row: level 1; second row: level 2) and diet (each diet shown in one color). All plotting conventions are consistent with Figure 5.

but it is $\geq 35\%$ for every diet. The first eigenfunction at the second level, $\widehat{\phi}_1^{(2)}(t)$, is also nearly constant with a small curvature and low sampling variability. This FPC explains between 25–33% of the total variability according to Figure 7, indicating that a constant shift is the main source of variation in glucose responses both among and within participants. The second eigenfunction at the meal level, $\widehat{\phi}_2^{(2)}(t)$, explains 10–25% of the total variability and has an *S* pattern. As in the single-level case, larger scores on $\widehat{\phi}_2^{(2)}(t)$ correspond to lower pre- and immediately post-prandial glucose, then increasingly larger response one to four hours after the meal. The eigenfunctions $\widehat{\phi}_2^{(1)}(t), \widehat{\phi}_3^{(2)}(t)$ capture higher-order glycemic reaction patterns and explain much smaller proportions of variability ($\leq 10\%$).

As in the single level case, the DASH4D/lower sodium diet exhibits less variability among subject-specific glucose response (compare first row, first column in Figure 7 to the first panel in Figure 5). This diet also has lower meal-to-meal variability, evident in the second row, first column of Figure 7. Across all diets, the second eigenvalues at the subject level are very small, particularly compared to the first two eigenvalues at the meal level (compare the first row, first column and second row, first column panels in Figure 7). This suggests that most variability can be partitioned in a constant vertical shift at the subject level and more complex meal-to-meal variation.

Each FAST MFPCA model takes ≈ 6 minutes to run 5000 iterations on a standard laptop, with the first 2500 discarded as burn-in. We again utilize the routine described in Section 2.5 to assess convergence of the scores and FPCs at both levels. This requires aligning each level separately. Final Gelman-Rubin statistics were ≤ 1.02 .

6 Discussion

Standard implementations of FPCA use a two-step procedure: (1) diagonalize a smooth estimate of the observed data covariance; and (2) conduct inference conditional on the FPC estimates from the first step. This does not account for sampling variability in the FPCs, which could be quite large for low to moderate signal-to-noise. Our approach is a single step joint Bayesian model that treats PCs as parameters in the model, which combines the orthogonal spline expansion from Ye (2024), the polar decomposition-based parameter expansion from Jauch et al. (2021), and stabilizing constraints to efficiently jointly model all FPCA model components. Combining the right ingredients led to FAST, a stable, replicable, and easy to implement methodology. The central element of FAST is expressing the FPCs in terms of an orthonormal spline basis. This is different from the approach in Ye (2024), as this spline basis: (1) is orthonormal in $L^2([0, 1])$, rather than in a vector sense; and (2) retains the computational efficiency of B-splines (Liu et al., 2020). This spline expansion simplifies the problem of sampling the high dimensional FPCs to sampling a low dimensional spline coefficients. The FPC spline coefficient matrix must be orthonormal to produce the corresponding FPC samples. This is done using the polar decomposition parameter expansion of Jauch et al. (2021), applying the technique to the coefficient matrix rather than the data level FPCs.

FAST performs as well or better than all existing methods, while being highly computational efficient and having excellent mixing properties. Moreover, the implementation of FAST within **STAN**, or equivalent software, allows for a widespread use of methods and requires only small adjustments for when tailoring the model for other applications.

Many questions remain, including: (1) generalizability to non-Gaussian, multivariate, sparse, and longitudinal functional data; (2) theoretical guarantees and non-uniform priors on the FPC parameter Stiefel manifold; (3) eigenbasis dimension estimation; and (4) further computational improvements, possibly through adaptive sampling.

References

Barua, S., A Wierzchowska-McNew, R., Deutz, N. E. P., and Sabharwal, A. (2022). Discordance between postprandial plasma glucose measurement and continuous glucose monitoring. *The American Journal of Clinical Nutrition*, 116(4):1059–1069.

Brumback, B., Ruppert, D., and Wand, M. (1999). Comment on variable selection and function estimation in additive nonparametric regression using data-based prior by Shively, Kohn, and Wood. *Journal of the American Statistical Association*, 94(447):794–797.

Carpenter, B., Gelman, A., Hoffman, M. D., Lee, D., Goodrich, B., Betancourt, M., Brubaker, M., Guo, J., Li, P., and Riddell, A. (2017). Stan: A Probabilistic Programming Language. *Journal of Statistical Software*, 76:1–32.

Chikuse, Y. (2003). *Statistics on Special Manifolds*, volume 174 of *Lecture Notes in Statistics*. Springer, New York, NY. Edited by Bickel, P. and Diggle, P. and Fienberg, S. and Krickeberg, K. and Olkin, I. and Wermuth, N. and Zeger, S.

Crainiceanu, C., Ruppert, D., and Wand, M. (2005). Bayesian analysis for penalized spline regression using winbugs. *Journal of Statistical Software*, 14(14):1–24.

Crainiceanu, C. M. and Goldsmith, A. J. (2010). Bayesian Functional Data Analysis Using WinBUGS. *Journal of Statistical Software*, 32:1–33.

Crainiceanu, C. M., Goldsmith, J., Leroux, A., and Cui, E. (2024). *Functional Data Analysis with R*. Chapman and Hall/CRC.

Craven, P. and Wahba, G. (1979). Smoothing noisy data with spline functions. *Numerische Mathematik*, 31:377–403.

Cui, E., Li, R., Crainiceanu, C. M., and Xiao, L. (2023). Fast Multilevel Functional Principal Component Analysis. *Journal of computational and graphical statistics : a joint publication of American Statistical Association, Institute of Mathematical Statistics, Interface Foundation of North America*, 32(2):366–377.

Di, C.-Z., Crainiceanu, C. M., Caffo, B. S., and Punjabi, N. M. (2009). Multilevel functional principal component analysis. *The Annals of Applied Statistics*, 3(1):458–488.

Fang, M., Wang, D., Rebholz, C. M., Echouffo-Tcheugui, J. B., Tang, O., Wang, N.-Y., Mitchell, C. M., Pilla, S. J., Appel, L. J., and Selvin, E. (2025). DASH4D diet for glycemic control and glucose variability in type 2 diabetes: a randomized crossover trial. *Nature Medicine*. Status: In press.

Garber, A. J. (2012). Postprandial Dysmetabolism and the Heart. *Heart Failure Clinics*, 8(4):563–573.

Gelman, A. and Rubin, D. B. (1992). Inference from Iterative Simulation Using Multiple Sequences. *Statistical Science*, 7(4):457–472. Publisher: Institute of Mathematical Statistics.

Goldsmith, J., Greven, S., and Crainiceanu, C. (2013). Corrected confidence bands for functional data using principal components. *Biometrics*, 69(1):41–51.

Goldsmith, J., Zipunnikov, V., and Schrack, J. (2015). Generalized Multilevel Function-on-Scalar Regression and Principal Component Analysis. *Biometrics*, 71(2):344–353.

Greven, S., Crainiceanu, C., Caffo, B., and Reich, D. (2010). Longitudinal functional principal component analysis. *Electronic journal of statistics*, 4:1022–1054.

Hershon, K. S., Hirsch, B. R., and Odugbesan, O. (2019). Importance of Postprandial Glucose in Relation to A1C and Cardiovascular Disease. *Clinical Diabetes : A Publication*

of the American Diabetes Association, 37(3):250–259.

Hoff, P. D. (2009). Simulation of the Matrix Bingham–von Mises–Fisher Distribution, With Applications to Multivariate and Relational Data. *Journal of Computational and Graphical Statistics*, 18(2):438–456.

James, G., Hastie, T., and Sugar, C. (2000). Principal component models for sparse functional data. *Biometrika*, 87(3):587–602.

James, I. (1976). *The Topology of Stiefel Manifolds*. Cambridge University Press.

Jauch, M., Hoff, P. D., and Dunson, D. B. (2021). Monte Carlo Simulation on the Stiefel Manifold via Polar Expansion. *Journal of Computational and Graphical Statistics*, 30(3):622–631.

Karhunen, K. (1947). Über lineare Methoden in der Wahrscheinlichkeitsrechnung. *Annals of the Academy of Science Fennicae*, 37(Series A. I. Mathematics-Physics):1–79.

Kimeldorf, G. and Wahba, G. (1970). A correspondence between bayesian estimation on stochastic processes and smoothing by splines. *The Annals of Mathematical Statistics*, 41(2):495–502.

Kosambi, D. (1943). Statistics in function space. *Journal of the Indian Mathematical Society*, 7:77–88.

Li, Y., Wang, N., and Carroll, R. J. (2013). Selecting the Number of Principal Components in Functional Data. *Journal of the American Statistical Association*, 108(504):1284–1294. Publisher: ASA Website eprint: <https://doi.org/10.1080/01621459.2013.788980>.

Liu, X., Nassar, H., and Podgórski, K. (2020). Splinets – efficient orthonormalization of the B-splines. arXiv:1910.07341.

Liu, Z. and Guo, W. (2012). Functional mixed effects models. *WIREs Computational Statistics*, 4(6):527–534.

Loève, M. (1978). *Probability Theory*, volume II of *Graduate Texts in Mathematics*. Springer-Verlag, 4th edition.

Mardia, K. and Khatri, C. (1977). Uniform distribution on a stiefel manifold. *Journal of Multivariate Analysis*, 7(3):468–473.

Meng, R. and Bouchard, K. E. (2024). Bayesian inference of structured latent spaces from neural population activity with the orthogonal stochastic linear mixing model. *PLOS Computational Biology*, 20(4):e1011975.

Nolan, T. H., Goldsmith, J., and Ruppert, D. (2023). Bayesian Functional Principal Components Analysis via Variational Message Passing with Multilevel Extensions. *Bayesian Analysis*, -1(-1):1–27.

O’Sullivan, F. (1986). A statistical perspective on ill-posed inverse problems (with discussion). *Statistical Science*, 1(4):505–527.

Park, H. G. (2025). Bayesian estimation of covariate assisted principal regression for brain functional connectivity. *Biostatistics*, 26(1):kxae023.

Peng, J. and Paul, D. (2009). A Geometric Approach to Maximum Likelihood Estimation of the Functional Principal Components From Sparse Longitudinal Data. *Journal of Computational and Graphical Statistics*, 18(4):995–1015.

Pilla, S. J., Yeh, H.-C., et al. (2025). Dietary Patterns, Sodium Reduction, and Blood Pressure in Type 2 Diabetes: The DASH4D Randomized Clinical Trial. *JAMA Internal Medicine*.

Reiss, P. T. and Ogden, R. T. (2007). Functional Principal Component Regression and

Functional Partial Least Squares. *Journal of the American Statistical Association*, 102(479):984–996.

Rice, J. A. and Wu, C. O. (2001). Nonparametric Mixed Effects Models for Unequally Sampled Noisy Curves. *Biometrics*, 57(1):253–259.

Ruppert, D. (2002). Selecting the Number of Knots for Penalized Splines. *Journal of Computational and Graphical Statistics*, 11(4):735–757.

Ruppert, D., Wand, M., and Carroll, R. (2003). *Semiparametric Regression*. Cambridge Series in Statistical and Probabilistic Mathematics. Cambridge University Press.

Röhling, M., Martin, T., Wonnemann, M., Kragl, M., Klein, H. H., Heinemann, L., Martin, S., and Kempf, K. (2019). Determination of Postprandial Glycemic Responses by Continuous Glucose Monitoring in a Real-World Setting. *Nutrients*, 11(10):2305.

Shi, M., Weiss, R. E., and Taylor, J. M. G. (1996). An Analysis of Paediatric CD4 Counts for Acquired Immune Deficiency Syndrome Using Flexible Random Curves. *Journal of the Royal Statistical Society Series C: Applied Statistics*, 45(2):151–163.

Shou, H., Zipunnikov, V., Crainiceanu, C. M., and Greven, S. (2015). Structured Functional Principal Component Analysis. *Biometrics*, 71(1):247–257.

Staniswalis, J. G., , and Lee, J. J. (1998). Nonparametric Regression Analysis of Longitudinal Data. *Journal of the American Statistical Association*, 93(444):1403–1418.

Team, S. D. (2025). Stan modeling language users guide and reference manual 2.36.

Wahba, G. (1983). Bayesian “Confidence Intervals” for the Cross-Validated Smoothing Spline. *Journal of the Royal Statistical Society: Series B*, 45(1):133–150.

Wang, D., Mu, S. Z., Tang, O., Echouffo-Tcheugui, J. B., Mitchell, C. M., Fang, M., Rooney, M. R., Yeh, H.-C., Rebholz, C. M., Pilla, S. J., Appel, L. J., and Selvin, E. (2025). Design of the Continuous Glucose Monitoring (CGM) Study in the Dietary Approaches to Stop Hypertension for Diabetes Trial (DASH4D-CGM). *Contemporary Clinical Trials*, 151:107845.

Wood, S. (2006). *Generalized Additive Models: An Introduction with R*. Chapman and Hall/CRC.

Xiao, L., Zipunnikov, V., Ruppert, D., and Crainiceanu, C. (2016). Fast Covariance Estimation for High-dimensional Functional Data. *Statistics and computing*, 26(1):409–421.

Yao, F., Müller, H.-G., and Wang, J.-L. (2005). Functional Data Analysis for Sparse Longitudinal Data. *Journal of the American Statistical Association*, 100(470):577–590.

Ye, J. (2024). Functional principal component models for sparse and irregularly spaced data by Bayesian inference. *Journal of Applied Statistics*, 51(7):1287–1317.

Zhou, L., Huang, J. Z., Martinez, J. G., Maity, A., Baladandayuthapani, V., and Carroll, R. J. (2010). Reduced Rank Mixed Effects Models for Spatially Correlated Hierarchical Functional Data. *Journal of the American Statistical Association*, 105(489):390–400.

Zhou, X., Cui, E., Sartini, J., and Crainiceanu, C. (2025). Prediction Inference Using Generalized Functional Mixed Effects Models. arXiv:2501.07842.

Zipunnikov, V., Caffo, B., Yousem, D., Davatzikos, C., Schwartz, B., and Crainiceanu, C. (2011). Multilevel functional principal component analysis for high-dimensional data. *Journal of Computational and Graphical Statistics*, 20(4):852–873.

SUPPLEMENTAL MATERIAL

S1 Penalty matrix \mathbf{P}_α

Recall we chose a posterior penalty approximating $\alpha \int f^2(t)dt + (1 - \alpha) \int \{f''(t)\}^2 dt$. For spline parameters θ such that $f(t) \approx \mathbf{B}(t)\theta$, there exist unique penalty matrices $\mathbf{P}_0, \mathbf{P}_2$ such that $\int f^2(t)dt \approx \theta^t \mathbf{P}_0 \theta$ and $\int \{f''(t)\}^2 dt \approx \theta^t \mathbf{P}_2 \theta$ (Craven and Wahba, 1979; Kimeldorf and Wahba, 1970; O’Sullivan, 1986; Wahba, 1983). We follow Goldsmith et al. (2015) and define $\mathbf{P}_\alpha = \alpha \mathbf{P}_0 + (1 - \alpha) \mathbf{P}_2$. This allows us to write the final penalty using a single quadratic form:

$$\begin{aligned} \alpha \int f^2(t)dt + (1 - \alpha) \int \{f''(t)\}^2 dt &\approx \alpha \theta^t \mathbf{P}_0 \theta + (1 - \alpha) \theta^t \mathbf{P}_2 \theta \\ &= \theta^t (\alpha \mathbf{P}_0 + (1 - \alpha) \mathbf{P}_2) \theta \\ &= \theta^t \mathbf{P}_\alpha \theta \end{aligned}$$

We proceed by defining both of the penalty components $\mathbf{P}_0, \mathbf{P}_2$ separately, as \mathbf{P}_α is just a linear combination of these matrices. Let $\mathbf{B}(t) = [b_1(t) | \dots | b_Q(t)]$ represent the basis functions, chosen to be orthonormal in $L^2([0, 1])$. First, we define the zero-order penalty \mathbf{P}_0 element-wise. This derivation leverages the orthonormal definition of the $b_i(t)$.

$$\begin{aligned} (\mathbf{P}_0)_{ij} &= \int_0^1 \int_0^1 b_i(t) b_j(t) dt \\ &= \begin{cases} 1 & \text{when } i = j \\ 0 & \text{otherwise} \end{cases} \end{aligned}$$

The resulting matrix $\mathbf{P}_0 = \mathbf{I}_Q$ by the definition of the basis $\mathbf{B}(t)$. This clearly indicates the role of this component (when non-zero) in ensuring the non-singularity of the final penalty \mathbf{P}_α , similar to adding a ridge penalty in the context of regression.

Next, we define the more central “wigginess” penalty \mathbf{P}_2 . For this penalty, based on the squared second derivative, we introduce the second derivatives of the basis $\mathbf{B}(T)$: $\mathbf{B}''(t) = [b_1''(t) | \dots | b_Q''(t)]$. We are able to quickly retrieve these derivatives using the properties of B-splines, from which the default Splinet basis is constructed (Liu et al., 2020). The elements of \mathbf{P}_2 are as follows.

$$(\mathbf{P}_2)_{ij} = \int_0^1 \int_0^1 b_i''(t) b_j''(t) dt$$

We approximate these quantities using numerical integration based upon Gaussian quadrature.

Combining \mathbf{P}_0 and \mathbf{P}_2 in linear combination produces the penalty \mathbf{P}_α , which will be non-degenerate when $\alpha > 0$ (the weight of the absolute penalty is non-zero).

S2 Joint and conditional posteriors

We begin by enumerating the model likelihood and parameter priors explicitly. We use $\Gamma(a, b)$ to denote the gamma distribution with shape a and rate b , $\Gamma^{-1}(a, b)$ to denote the inverse gamma distribution with shape a and scale b , $N(\mu, \sigma^2)$ to indicate the normal distribution with mean μ and variance σ^2 , and $MVN(\boldsymbol{\mu}, \boldsymbol{\Sigma})$ to denote the multivariate normal distribution with mean $\boldsymbol{\mu}$ and variance-covariance $\boldsymbol{\Sigma}$. Throughout, I_A denotes the identity matrix of dimension A .

Variance Component Priors:

Prior distributions of the variance and smoothing parameter components are as follows.

$$\begin{aligned}\sigma^2 &\sim \Gamma^{-1}(\alpha_\sigma, \beta_\sigma) \\ \lambda_k &\sim \Gamma^{-1}(\alpha_\lambda, \beta_\lambda) \quad \forall k = 1, \dots, K \\ h_\mu &\sim \Gamma(\alpha_\mu, \beta_\mu) \\ h_k &\sim \Gamma(\alpha_\psi, \beta_\psi) \quad \forall k = 1, \dots, K\end{aligned}$$

We set nearly uninformative priors, $\alpha_\sigma, \alpha_\lambda, \alpha_\psi, \alpha_\mu = 0.001$ and $\beta_\sigma, \beta_\lambda, \beta_\psi, \beta_\mu = 0.001$.

We also enforce ordering of the eigenvalues, requiring the indicator $\mathbb{1}(\lambda_1 \geq \dots \geq \lambda_K)$.

Prior on w_μ :

FAST implements a smoothing prior on $\mu(t)$ through a posterior penalty on spline coefficients w_μ . For prior density $f(w_\mu)$, we have the following, where $\mathbf{R}(\cdot)$ indicates matrix rank.

$$f(w_\mu) \propto h_\mu^{\mathbf{R}(\mathbf{P}_\alpha)/2} \exp \left\{ -\frac{h_\mu}{2} w_\mu^t \mathbf{P}_\alpha w_\mu \right\}$$

Prior on FPCs:

FAST implements a similar smoothing prior on the $\phi_k(t)$ through the spline coefficients ψ_k . For prior density $f(\psi_k)$, we have the following, where $\mathbf{R}(\cdot)$ indicates matrix rank.

$$f(\psi_k) \propto h_k^{\mathbf{R}(\mathbf{P}_\alpha)/2} \exp \left\{ -\frac{h_k}{2} \psi_k^t \mathbf{P}_\alpha \psi_k \right\}$$

For orthonormality of the FPCs, FAST requires the additional constraint that the matrix $\boldsymbol{\Psi} = [\psi_1 | \dots | \psi_K]$ is orthonormal. This requires introducing the indicator $\mathbb{1}(\boldsymbol{\Psi} \in \mathcal{V}_{K,Q})$ to the prior distribution, where $\mathcal{V}_{K,Q}$ is the Stiefel manifold of dimension $Q \times K$.

Prior on the Scores:

Score priors are as defined in FPCA according to the Kosambi-Karhunen-Loève decomposition: $\xi_{ik} \sim N(0, \lambda_k)$ for $i \in \{1, 2, \dots, N\}$ and $k \in \{1, 2, \dots, K\}$.

Model Likelihood:

We begin with notation. Let $Y_i \in \mathbb{R}^M$ represent the vector of data for participant i observed at the times $t \in \{t_1, \dots, t_M\}$. Correspondingly, let $\mathbf{B} \in \mathbb{R}^{M \times Q}$ be the orthonormal basis matrix evaluated at the same set of observation points. Using these definitions, the FPCA model likelihood contribution is as follows.

$$Y_i \sim MVN\{\mathbf{B}(w_\mu + \sum_{k=1}^K \xi_{ik}\psi_k), \sigma^2 I_M\}$$

Joint Posterior:

Given the likelihood and priors previously described, the posterior density of all model parameters given the data is proportional to the following. Throughout, we use the notation $f(X|\Theta)$ to represent the evaluation of density $f(\cdot)$ at point X with parameters Θ .

$$\begin{aligned} & \prod_{i=1}^N MVN\{Y_i|\mathbf{B}(w_\mu + \sum_{k=1}^K \xi_{ik}\psi_k), \sigma^2 I_M\} \times \Gamma^{-1}(\sigma^2|\alpha_\sigma, \beta_\sigma) \\ & \times \left\{ \prod_{k=1}^K N(\xi_{ik}|0, \lambda_k) \times \Gamma^{-1}(\lambda_k|\alpha_\lambda, \beta_\lambda) \times h_k^{\mathbf{R}(\mathbf{P}_\alpha)/2} \exp\left(-\frac{h_k}{2}\psi_k^t \mathbf{P}_\alpha \psi_k\right) \times \Gamma(h_k|\alpha_\psi, \beta_\psi) \right\} \\ & \times h_\mu^{\mathbf{R}(\mathbf{P}_\alpha)/2} \exp\left(-\frac{h_\mu}{2}w_\mu^t \mathbf{P}_\alpha w_\mu\right) \times \Gamma(h_\mu|\alpha_\mu, \beta_\mu) \times \mathbb{1}(\lambda_1 \geq \dots \geq \lambda_K) \times \mathbb{1}(\Psi \in \mathcal{V}_{Q,K}) \end{aligned} \tag{3}$$

Using this joint posterior form, we begin to derive the individual conditional posteriors for each component.

Smoothing Parameters:

First, we derive the conditional posterior for the smoothing parameter for the mean, h_μ , which we denote $f(h_\mu|\text{others})$.

$$\begin{aligned} f(h_\mu|\text{others}) & \propto h_\mu^{\mathbf{R}(\mathbf{P}_\alpha)/2} \exp\left(-\frac{h_\mu}{2}w_\mu^t \mathbf{P}_\alpha w_\mu\right) \times \Gamma(h_\mu|\alpha_\mu, \beta_\mu) \\ & \propto h_\mu^{\mathbf{R}(\mathbf{P}_\alpha)/2} \exp\left(-\frac{h_\mu}{2}w_\mu^t \mathbf{P}_\alpha w_\mu\right) \times h_\mu^{\alpha_\mu-1} \exp(-\beta_\mu h_\mu) \\ & \propto h_\mu^{\{\mathbf{R}(\mathbf{P}_\alpha)/2+\alpha_\mu\}-1} \exp\left\{-\left(\frac{w_\mu^t \mathbf{P}_\alpha w_\mu}{2} + \beta_\mu\right) h_\mu\right\} \end{aligned}$$

One can recognize the form of the gamma distribution in the last line above.

$$[h_\mu | \text{others}] \sim \Gamma(\mathbf{R}(\mathbf{P}_\alpha)/2 + \alpha_\mu, w_\mu^t \mathbf{P}_\alpha w_\mu/2 + \beta_\mu)$$

We can similarly derive the conditional posterior distribution for the general eigenfunction smoothing parameter h_k , which we denote $f(h_k | \text{others})$.

$$\begin{aligned} f(h_k | \text{others}) &\propto h_k^{\mathbf{R}(\mathbf{P}_\alpha)/2} \exp\left(-\frac{h_k}{2} \psi_k^t \mathbf{P}_\alpha \psi_k\right) \times \Gamma(h_k | \alpha_\psi, \beta_\psi) \\ &\propto h_k^{\mathbf{R}(\mathbf{P}_\alpha)/2} \exp\left(-\frac{h_k}{2} \psi_k^t \mathbf{P}_\alpha \psi_k\right) \times h_k^{\alpha_\psi - 1} \exp(-\beta_\psi h_k) \\ &\propto h_k^{\{\mathbf{R}(\mathbf{P}_\alpha)/2 + \alpha_\psi\} - 1} \exp\left\{-\left(\frac{\psi_k^t \mathbf{P}_\alpha \psi_k}{2} + \beta_\psi\right) h_k\right\} \end{aligned}$$

Once more, the form of the gamma distribution is clear in the final line above.

$$[h_k | \text{others}] \sim \Gamma(\mathbf{R}(\mathbf{P}_\alpha)/2 + \alpha_\psi, \psi_k^t \mathbf{P}_\alpha \psi_k/2 + \beta_\psi)$$

Noise variance σ^2 :

We derive the conditional posterior of σ^2 , denoted $f(\sigma^2 | \text{others})$, below.

$$\begin{aligned} f(\sigma^2 | \text{others}) &\propto \prod_{i=1}^N MVN\{Y_i | \mathbf{B}(w_\mu + \sum_{k=1}^K \xi_{ik} \psi_k), \sigma^2 I_M\} \times \Gamma^{-1}(\sigma^2 | \alpha_\sigma, \beta_\sigma) \\ &\propto \prod_{i=1}^N (\sigma^2)^{-M/2} \exp\left(-\frac{\|Y_i - \mathbf{B}(w_\mu + \sum_{k=1}^K \xi_{ik} \psi_k)\|^2}{2\sigma^2}\right) \times (\sigma^2)^{-\alpha_\sigma - 1} \exp\left(-\frac{\beta_\sigma}{\sigma^2}\right) \\ &\propto (\sigma^2)^{-(NM/2 + \alpha_\sigma) - 1} \exp\left\{-\frac{1}{\sigma^2} \left(\frac{1}{2} \sum_{i=1}^n \|Y_i - \mathbf{B}(w_\mu + \sum_{k=1}^K \xi_{ik} \psi_k)\|^2 + \beta_\sigma\right)\right\} \end{aligned}$$

The last line above is clearly the form of the inverse gamma distribution, with exact parameterization as follows:

$$[\sigma^2 | \text{others}] \sim \Gamma^{-1}\left(\frac{NM}{2} + \alpha_\sigma, \frac{1}{2} \sum_{i=1}^n \|Y_i - \mathbf{B}(w_\mu + \sum_{k=1}^K \xi_{ik} \psi_k)\|^2 + \beta_\sigma\right)$$

Eigenvalues λ_k :

The joint conditional posterior distribution of the eigenvalues λ_k , denoted $f(\lambda_1, \dots, \lambda_K | \text{others})$,

is derived below.

$$\begin{aligned}
f(\lambda_1, \dots, \lambda_K | \text{others}) &\propto \prod_{k=1}^K \prod_{i=1}^N N(\xi_{ik} | 0, \lambda_k) \times \Gamma^{-1}(\lambda_k | \alpha_\lambda, \beta_\lambda) \times \mathbb{1}(\lambda_1 \geq \dots \geq \lambda_K) \\
&\propto \prod_{k=1}^K \lambda_k^{-N/2} \exp\left(-\frac{1}{2\lambda_k} \sum_{i=1}^N \xi_{ik}^2\right) \times \lambda_k^{-\alpha_\lambda-1} \exp\left(-\frac{\beta_\lambda}{\lambda_k}\right) \times \mathbb{1}(\lambda_1 \geq \dots \geq \lambda_K) \\
&\propto \prod_{k=1}^K \lambda_k^{-(N/2+\alpha_\lambda)-1} \exp\left\{-\frac{1}{\lambda_k} \left(\frac{1}{2} \sum_{i=1}^N \xi_{ik}^2 + \beta_\lambda\right)\right\} \times \mathbb{1}(\lambda_1 \geq \dots \geq \lambda_K)
\end{aligned}$$

The above joint distribution has the form of independent inverse gamma distributions ($[\lambda_k | \text{others}] \sim \Gamma^{-1}(N/2 + \alpha_\lambda, \frac{1}{2} \sum_{i=1}^N \xi_{ik}^2 + \beta_\lambda)$), with the additional constraint that the λ_k be ordered. Sampling from this type of joint distribution is possible using ordered transforms and corresponding Jacobian transforms as described in the STAN documentation (Team, 2025).

Mean spline coefficients w_μ :

We derive the conditional posterior of w_μ , denoted $f(w_\mu | \text{others})$ as follows.

$$\begin{aligned}
f(w_\mu | \text{others}) &\propto \prod_{i=1}^N MVN\{Y_i | \mathbf{B}(w_\mu + \sum_{k=1}^K \xi_{ik} \psi_k), \sigma^2 I_M\} \times \exp\left(-\frac{h_\mu}{2} w_\mu^t \mathbf{P}_\alpha w_\mu\right) \\
&\propto \prod_{i=1}^N \exp\left\{-\frac{\|\mathbf{B}w_\mu - (Y_i - \mathbf{B} \sum_{k=1}^K \xi_{ik} \psi_k)\|^2}{2\sigma^2} - \frac{h_\mu}{2} w_\mu^t \mathbf{P}_\alpha w_\mu\right\} \\
&\propto \exp\left\{-\sum_{i=1}^N \frac{\|\mathbf{B}w_\mu\|^2 - 2\langle Y_i - \mathbf{B} \sum_{k=1}^K \xi_{ik} \psi_k, \mathbf{B}w_\mu \rangle}{2\sigma^2} - \frac{h_\mu}{2} w_\mu^t \mathbf{P}_\alpha w_\mu\right\}
\end{aligned}$$

We now introduce the shorthand $D_i = Y_i - \mathbf{B} \sum_{k=1}^K \xi_{ik} \psi_k$ to denote the residual between the data Y_i and the cumulative random effect $\mathbf{B} \sum_{k=1}^K \xi_{ik} \psi_k$. We continue using this notation.

$$\begin{aligned}
f(w_\mu | \text{others}) &\propto \exp\left\{-\sum_{i=1}^N \frac{\|\mathbf{B}w_\mu\|^2 - 2D_i^t \mathbf{B}w_\mu}{2\sigma^2} - w_\mu^t \frac{h_\mu \mathbf{P}_\alpha}{2} w_\mu\right\} \\
&\propto \exp\left\{-w_\mu^t \left(\sum_{i=1}^N \frac{\mathbf{B}^t \mathbf{B}}{2\sigma^2}\right) w_\mu + \left(\sum_{i=1}^N \frac{D_i^t \mathbf{B}}{\sigma^2}\right) w_\mu - w_\mu^t \frac{h_\mu \mathbf{P}_\alpha}{2} w_\mu\right\} \\
&\propto \exp\left\{-w_\mu^t \left(\frac{N\mathbf{B}^t \mathbf{B}}{2\sigma^2} + \frac{h_\mu \mathbf{P}_\alpha}{2}\right) w_\mu + \left(\sum_{i=1}^N \frac{D_i^t \mathbf{B}}{\sigma^2}\right) w_\mu\right\} \\
&\propto \exp\left[-\frac{1}{2} \left\{w_\mu^t \left(\frac{N\mathbf{B}^t \mathbf{B}}{\sigma^2} + h_\mu \mathbf{P}_\alpha\right) w_\mu - 2 \left(\sum_{i=1}^N \frac{D_i^t \mathbf{B}}{\sigma^2}\right) w_\mu\right\}\right]
\end{aligned}$$

Completing the square, we find that w_μ has a multivariate normal distribution

$$[w_\mu | \text{others}] \sim MVN\left\{\left(\frac{N\mathbf{B}^t\mathbf{B}}{\sigma^2} + h_\mu \mathbf{P}_\alpha\right)^{-1} \frac{1}{\sigma^2} \sum_{i=1}^N \mathbf{B}^t D_i, \left(\frac{N\mathbf{B}^t\mathbf{B}}{\sigma^2} + h_\mu \mathbf{P}_\alpha\right)^{-1}\right\}$$

Scores ξ_{ik} :

For arbitrary score ξ_{ik} (study participant i and FPC k), we derive the conditional posterior $f(\xi_{ik} | \text{others})$ as follows.

$$\begin{aligned} f(\xi_{ik} | \text{others}) &\propto MVN\{Y_i | \mathbf{B}(w_\mu + \sum_{p=1}^K \xi_{ip} \psi_p), \sigma^2 I_M\} \times N(\xi_{ik} | 0, \lambda_k) \\ &\propto \exp\left(-\frac{\|Y_i - \mathbf{B}(w_\mu + \sum_{p=1}^K \xi_{ip} \psi_p)\|^2}{2\sigma^2} - \frac{\xi_{ik}^2}{2\lambda_k}\right) \\ &\propto \exp\left(-\frac{\|Y_i - \mathbf{B}(w_\mu + \sum_{p \neq k}^K \xi_{ip} \psi_p) - \mathbf{B}\psi_k \xi_{ik}\|^2}{2\sigma^2} - \frac{\xi_{ik}^2}{2\lambda_k}\right) \end{aligned}$$

For the sake of conciseness, we now define the residual quantity $P_{ik} = Y_i - \mathbf{B}(w_\mu + \sum_{p \neq k}^K \xi_{ip} \psi_p)$, which can be thought of as the residual between $Y_i - \mathbf{B}w_\mu$ and the projection of $Y_i - \mathbf{B}w_\mu$ onto the FPCs other than k .

$$\begin{aligned} f(\xi_{ik} | \text{others}) &\propto \exp\left(-\frac{\|P_{ik} - \mathbf{B}\psi_k \xi_{ik}\|^2}{2\sigma^2} - \frac{\xi_{ik}^2}{2\lambda_k}\right) \\ &\propto \exp\left(-\frac{\|\mathbf{B}\psi_k\|^2 \xi_{ik}^2 - 2P_{ik}^t \mathbf{B}\psi_k \xi_{ik}}{2\sigma^2} - \frac{\xi_{ik}^2}{2\lambda_k}\right) \\ &\propto \exp\left[-\frac{1}{2} \left\{ \xi_{ik}^2 \left(\frac{\|\mathbf{B}\psi_k\|^2}{\sigma^2} + \frac{1}{\lambda_k} \right) - 2 \frac{P_{ik}^t \mathbf{B}\psi_k}{\sigma^2} \xi_{ik} \right\}\right] \end{aligned}$$

Completing the square, we find that ξ_{ik} has a normal distribution.

$$[\xi_{ik} | \text{others}] \sim N\left\{\left(\frac{\|\mathbf{B}\psi_k\|^2}{\sigma^2} + \frac{1}{\lambda_k}\right)^{-1} \frac{P_{ik}^t \mathbf{B}\psi_k}{\sigma^2}, \left(\frac{\|\mathbf{B}\psi_k\|^2}{\sigma^2} + \frac{1}{\lambda_k}\right)^{-1}\right\}$$

FPC Weights Ψ :

We derive the posterior distribution of the full matrix of FPC spline weights, denoted $f(\Psi | \text{others})$, below.

$$\begin{aligned} f(\Psi | \text{others}) &\propto \prod_{i=1}^N MVN\{Y_i | \mathbf{B}(w_\mu + \sum_{k=1}^K \xi_{ik} \psi_k), \sigma^2 I_M\} \times \prod_{k=1}^K h_k^{\mathbf{R}(\mathbf{P}_\alpha)/2} \exp\left(-\frac{h_k}{2} \psi_k^t \mathbf{P}_\alpha \psi_k\right) \times \mathbb{1}(\Psi \in \mathcal{V}_{K,Q}) \\ &\propto \exp\left(-\frac{1}{2\sigma^2} \sum_{i=1}^N \|Y_i - \mathbf{B}(w_\mu + \sum_{k=1}^K \xi_{ik} \psi_k)\|^2\right) \times \exp\left(-\frac{1}{2} \sum_{k=1}^K h_k \psi_k^t \mathbf{P}_\alpha \psi_k\right) \times \mathbb{1}(\Psi \in \mathcal{V}_{K,Q}) \end{aligned}$$

We now introduce the shorthand notation: score vector $\xi_i = \{\xi_{i1}, \dots, \xi_{iK}\}^t \in \mathbb{R}^K$, diagonal smoothing parameter matrix $\mathbf{H} = \text{diag}(h_1, \dots, h_K)$, and residual vector $R_i = Y_i - \mathbf{B}w_\mu$. Let $\text{tr}(\cdot)$ indicate the trace of a matrix.

$$\begin{aligned}
f(\Psi | \text{others}) &\propto \exp \left\{ -\frac{1}{2\sigma^2} \sum_{i=1}^N \|R_i - \mathbf{B}\Psi\xi_i\|^2 - \frac{1}{2} \text{tr}(\mathbf{H}\Psi^t \mathbf{P}_\alpha \Psi) \right\} \times \mathbb{1}(\Psi \in \mathcal{V}_{K,Q}) \\
&\propto \exp \left\{ -\frac{1}{2\sigma^2} \sum_{i=1}^N (\|R_i\|^2 - 2R_i^t \mathbf{B}\Psi\xi_i + \|\mathbf{B}\Psi\xi_i\|^2) - \frac{1}{2} \text{tr}(\mathbf{H}\Psi^t \mathbf{P}_\alpha \Psi) \right\} \times \mathbb{1}(\Psi \in \mathcal{V}_{K,Q}) \\
&\propto \exp \left\{ -\frac{1}{2\sigma^2} \sum_{i=1}^N (-2R_i^t \mathbf{B}\Psi\xi_i + \|\mathbf{B}\Psi\xi_i\|^2) - \frac{1}{2} \text{tr}(\mathbf{H}\Psi^t \mathbf{P}_\alpha \Psi) \right\} \times \mathbb{1}(\Psi \in \mathcal{V}_{K,Q}) \\
&\propto \exp \left\{ -\frac{1}{2\sigma^2} \left(-2 \sum_{i=1}^N R_i^t \mathbf{B}\Psi\xi_i + \sum_{i=1}^N \|\mathbf{B}\Psi\xi_i\|^2 \right) - \frac{1}{2} \text{tr}(\mathbf{H}\Psi^t \mathbf{P}_\alpha \Psi) \right\} \times \mathbb{1}(\Psi \in \mathcal{V}_{K,Q})
\end{aligned}$$

We now introduce more notation: score matrix $\Xi \in \mathbb{R}^{N \times K}$, where each row is the score vector ξ_i , and residual matrix $\mathbf{R} \in \mathbb{R}^{N \times M}$, where each row is the residual vector R_i .

$$\begin{aligned}
f(\Psi | \text{others}) &\propto \exp \left[-\frac{1}{2\sigma^2} \left\{ -2 \text{tr}(\mathbf{R}^t \mathbf{B}\Psi \Xi) + \text{tr}(\Xi^t \Psi^t \mathbf{B}^t \mathbf{B}\Psi \Xi) \right\} - \frac{1}{2} \text{tr}(\mathbf{H}\Psi^t \mathbf{P}_\alpha \Psi) \right] \times \mathbb{1}(\Psi \in \mathcal{V}_{K,Q}) \\
&\propto \exp \left\{ \frac{1}{\sigma^2} \text{tr}(\mathbf{R}^t \mathbf{B}\Psi \Xi) - \frac{1}{2\sigma^2} \text{tr}(\Xi^t \Psi^t \mathbf{B}^t \mathbf{B}\Psi \Xi) - \frac{1}{2} \text{tr}(\mathbf{B}\Psi^t \mathbf{P}_\alpha \Psi) \right\} \times \mathbb{1}(\Psi \in \mathcal{V}_{K,Q}) \\
&\propto \exp \left\{ \frac{1}{\sigma^2} \text{tr}(\Xi \mathbf{R}^t \mathbf{B}\Psi) - \frac{1}{2\sigma^2} \text{tr}(\Xi \Xi^t \Psi^t \mathbf{B}^t \mathbf{B}\Psi) - \frac{1}{2} \text{tr}(\mathbf{B}\Psi^t \mathbf{P}_\alpha \Psi) \right\} \times \mathbb{1}(\Psi \in \mathcal{V}_{K,Q}) \\
&\propto \exp \left\{ \text{tr} \left(\frac{\Xi \mathbf{R}^t \mathbf{B}\Psi}{\sigma^2} - \frac{\Xi \Xi^t \Psi^t \mathbf{B}^t \mathbf{B}\Psi}{2\sigma^2} - \frac{\mathbf{B}\Psi^t \mathbf{P}_\alpha \Psi}{2} \right) \right\} \times \mathbb{1}(\Psi \in \mathcal{V}_{K,Q})
\end{aligned}$$

The final line above is the form found in Result 1, which is not of a known distributional family.

S3 Simulation results

S3.1 Background

All code used for data simulation and subsequent model fitting can be found at this GitHub repository. We compare the data generating model used in S1, meant to imitate the CGM data from DASH4D, to the actual FPCs estimated from the real CGM data in Figure S1.

While the FPCs used in our generative model for S1 (“Simulation”) differ from the FPCs estimated from the mean postprandial CGM responses (“Estimated”) in several non-trivial

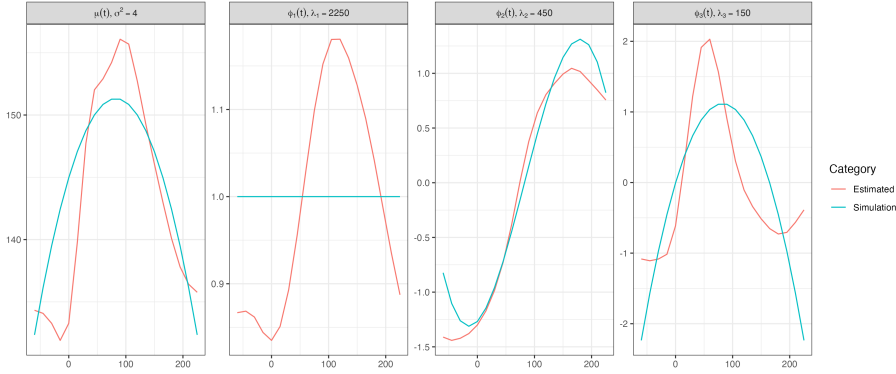


Figure S1: Comparison between the generative FPCs used in simulations (“Simulation”) and estimates from fitting FPCA to the CGM data (“Estimated”). The CGM data used was the by-participant mean postprandial response curves from the DASH4D study.

aspects, we choose them for their balance between adequate approximation and simplicity of generation. We built the “Simulation” bases using linear combinations of the Legendre polynomials, a known orthonormal basis of $L^2([0, 1])$, to enhance reproducibility.

S3.2 Fixed effects comparison

We compare the fixed effects estimates of $\mu(t)$ produced by FAST to those from the 3 comparator methods. We compare ISE of the posterior estimate and aggregate coverage of equal-tailed 95% credible intervals, each calculated using the same procedures outlined for the FPCs in Section 4.

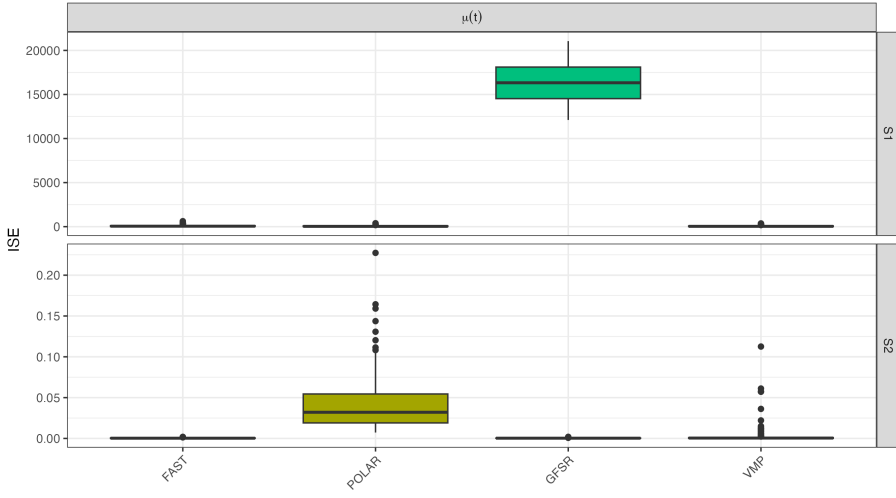


Figure S2: Boxplots of ISE for the mean $\mu(t)$ by estimation method. Row indicates simulation scenario, S1 then S2.

Figure S2 demonstrates the ISE of $\mu(t)$ by method, where row indicates simulation scenario. FAST produces estimates of $\mu(t)$ with ISE similar or superior to those of the

comparator methods. GFSR notably has substantial error for S1. Based upon further analysis of this phenomenon, we believe this is due to projection of the fixed effect onto the two FPCs $\phi_1(t), \phi_3(t)$, as described in Section 4.

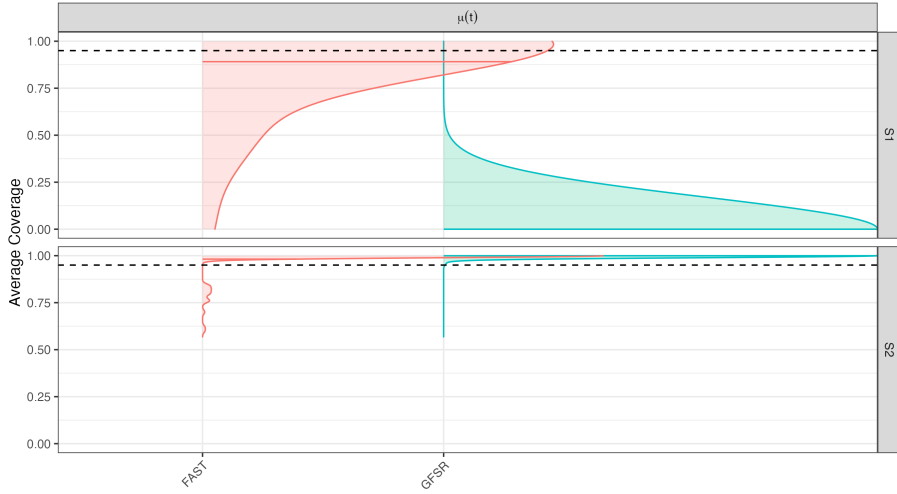


Figure S3: Kernel smoother of coverage probabilities of 95% credible intervals of the true mean $\mu(t)$ for FAST and GFSR. Row indicates simulation scenario, S1 then S2. Distribution means: horizontal solid lines; nominal 95% level: horizontal dotted lines.

Figure S3 visualizes kernel smooths of equal-tailed 95% credible interval coverage for FAST and GFSR, where row again indicates simulation scenario. We do not include POLLAR and VMP in this comparison, as neither produces posterior inferences upon the mean function $\mu(t)$. Inference is similar between FAST and GFSR for the canonical scenario S2, but coverage is far closer to nominal for FAST in the CGM-based S1.

S3.3 Score comparison

We also compare FAST to existing Bayesian FPCA implementations in their estimation of the score ξ_{ik} . Metrics of interest include mean squared error (MSE) of posterior mean estimates and mean coverage of equal-tail 95% credible intervals, each aggregated over curves i for each combination of FPC k and simulation.

Figure S4 visualizes the distribution of score MSE over simulations. FAST is has consistently similar or lower MSE when compared to the existing methods. GFSR has much larger MSE for those scores associated with $\phi_1(t)$ in S1. The order of this MSE is close to $140^2 = 19600$, supporting our previous assertion that the mean $\mu(t)$ is being projected onto $\phi_1(t)$ and $\phi_3(t)$ by this implementation.

Figure S5 displays the kernel smooth of the vectors of coverage proportions for FAST and all 3 comparator methods by FPC (columns) and simulation scenario (rows). FAST is the only implementation which produces consistently close to nominal coverage for all FPCs under both scenarios.

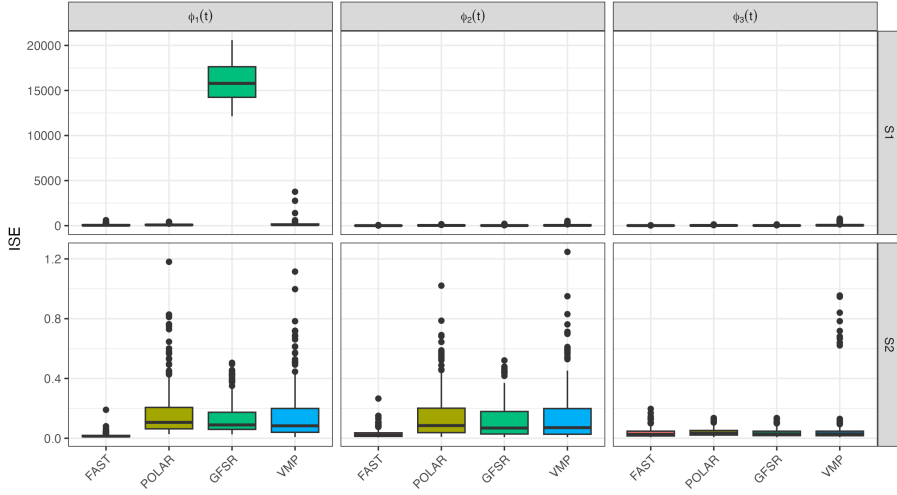


Figure S4: Boxplots of MSE for the scores ξ_{ik} by estimation method. Column indicates FPC, and row indicates simulation scenario, S1 then S2.

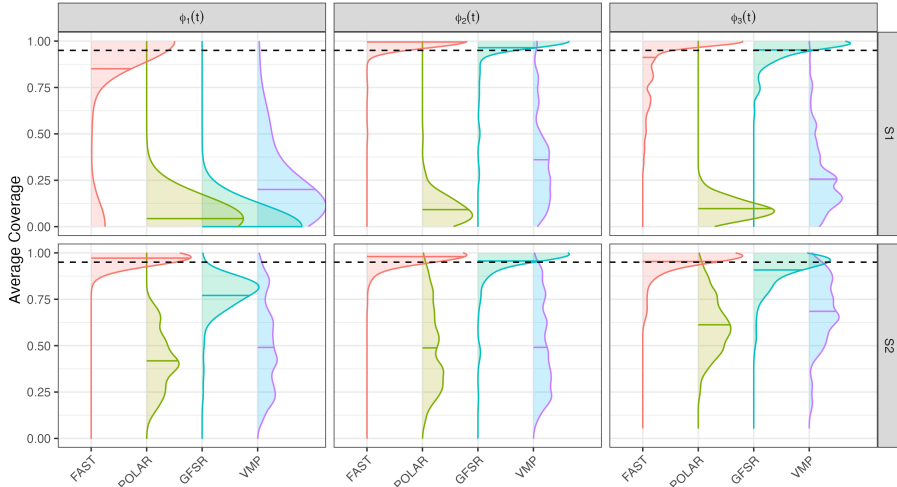


Figure S5: Kernel smoother of coverage probabilities of 95% credible intervals of the true scores, ξ_{ik}^b , for FAST, GFSR, POLAR, and VMP. First row: S1; second row: S2. Each column: corresponding eigenfunction. Distribution means: horizontal solid lines; nominal 95% level: horizontal dotted lines.

S3.4 Multilevel extension

We perform a simple 2-level simulation study to assess performance of the multilevel extension of FAST in comparison to GFSR. This simulation includes 50 groups at the first level ($N = 50$), each with 5 functional observations ($\forall i, J_i = 5$) for a total of 250 functions. We are only able to compare against GFSR due to both POLAR and VMP having no available multilevel extension. We use a well-known and frequently used multilevel simulation scenario for our study, where the FPCs are orthogonal within level but not between. All explicit details are provided below (Cui et al., 2023).

Multilevel Scenario

$$\begin{aligned}\phi_k^{(1)}(t) &= \{\sqrt{2} \sin(2\pi t), \sqrt{2} \cos(2\pi t), \sqrt{2} \sin(4\pi t), \sqrt{2} \cos(4\pi t)\}; \quad \lambda_k^{(1)} = 0.5^{k-1} \\ \phi_l^{(2)}(t) &= \{1, \sqrt{3}(2t-1), \sqrt{5}(6t^2-6t+1), \sqrt{7}(20t^3-30t^2+12t-1)\}; \quad \lambda_l^{(2)} = 0.5^{l-1} \\ \mu(t) &= 0; \quad \sigma^2 = 1\end{aligned}$$

We first present the integrated squared error (ISE) of the FPCs $\phi_k^{(1)}(t), \phi_l^{(2)}(t)$. We calculate this measure using the same procedure detailed in Section 4. Each panel corresponds to one of the eigenfunctions, with column indicating index and row indicating level.

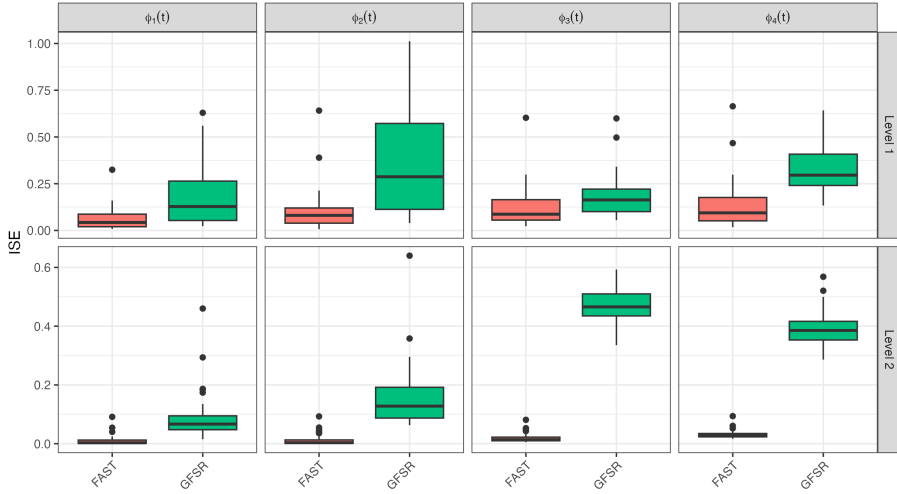


Figure S6: Boxplots of FPC ISE for FAST and GFSR from the multilevel simulations. Row indicates hierarchical level, while columns correspond to FPCs.

Figure S6 indicates uniformly lower ISE for FAST as compared to GFSR. These differences can be extreme, see for example the third and fourth FPCs at the visit level, $\phi_3^{(2)}(t), \phi_4^{(2)}(t)$.

We next consider FPC coverage according to the point-wise equal-tailed 95% credible intervals produced by FAST and GFSR. As in Section 4, we estimate coverage probability using the proportion of time points which are covered for each simulated dataset, visualizing the result with a kernel smooth in Figure S7. We include on this Figure the mean of each coverage distribution (horizontal solid lines) and the nominal coverage 95% coverage level (horizontal dotted lines).

Similar to the single-level simulations, we find that FAST produces nearly nominal coverage for all FPCs. In comparison, GFSR does not cover the eigenfunctions at the visit level well. For these FPCs, mean coverage ranges from ≈ 0.15 to ≈ 0.7 .

This disparity in coverage extends to the scores at both levels, ξ_{ik} and ζ_{ijk} , as can be observed in Figure S8. We estimate score coverage in the same fashion illustrated in Section 4. For each simulated dataset $b \leq B$, we calculate the 95% credible intervals

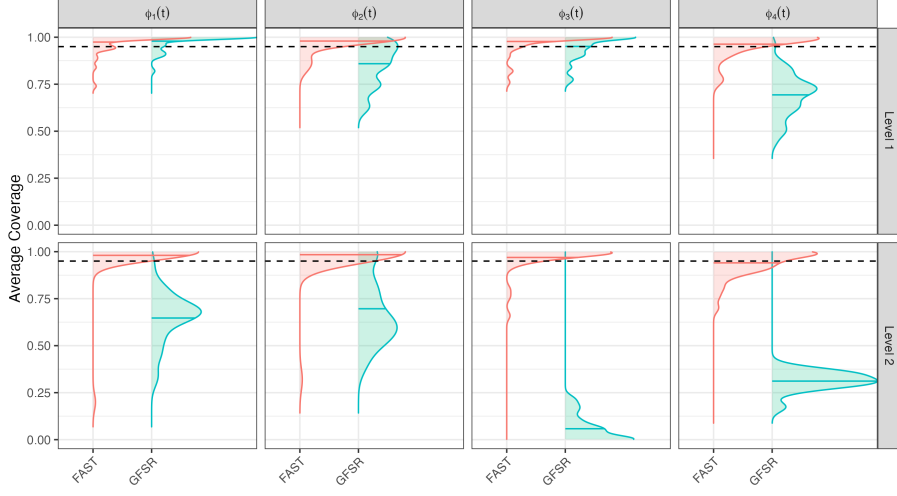


Figure S7: Kernel smoother of coverage probabilities of 95% credible intervals of the true FPCs for FAST and GFSR from the multilevel simulations. Row indicates hierarchical level, while columns correspond to FPCs. The horizontal dotted lines indicate the nominal 95% level.

for each individual $\xi_{ik}^b, \zeta_{ijk}^b$ from the posterior samples. We then estimate the coverage probability by aggregating the coverage indicators by the corresponding eigenfunction. Figure S8 visualizes the kernel smooths of the corresponding vectors of coverage, complete with distribution mean (solid horizontal lines) and nominal level (dashed horizontal lines). As was the case for the functional components presented in Figure S7, nominal coverage of the scores is uniquely achieved by FAST. GFSR achieves lower mean coverages, particularly for the FPCs $\phi_1(t)$ at each level.

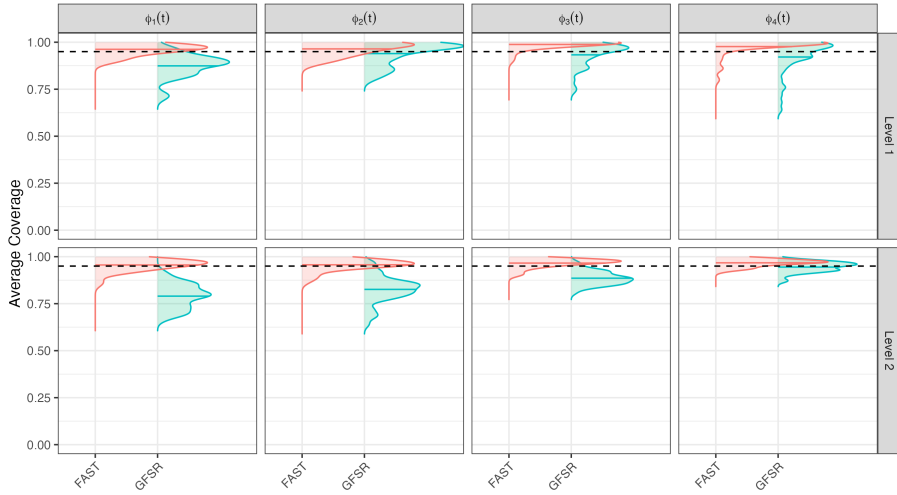


Figure S8: Kernel smoother of coverage probabilities of 95% credible intervals of the true scores, $\xi_{ik}^b, \zeta_{ijk}^b$, for FAST and GFSR from the multilevel simulations. Row indicates hierarchical level, while columns correspond to FPCs. The horizontal dotted lines indicate the nominal 95% level.

S4 Simulation sensitivity analyses

For each sensitivity analysis, we vary one of the core hyper-parameters from the set K (number of FPCs), Q (dimension of the spline basis), and α (proportion of the penalty which is absolute rather than second order). The default values are $K = 3$ (the true number of FPCs), $Q = 20$, and $\alpha = 0.1$. All sensitivity analyses are conducted within simulation scenarios S1 and S2 described in Section 4. We finally evaluate the effect of each of these sensitivity analyses on the computational efficiency of FAST in Section S4.4.

S4.1 Chosen number of FPCs K

We first vary the fixed number of FPCs K which FAST estimates. The true value is $K = 3$ for scenarios S1 and S2, so we vary between $K = 2$ and $K = 6$ to understand the effects of insufficient and excessive K . We evaluate FAST under each K value using ISE and coverage of the FPCs as described in Section 4.

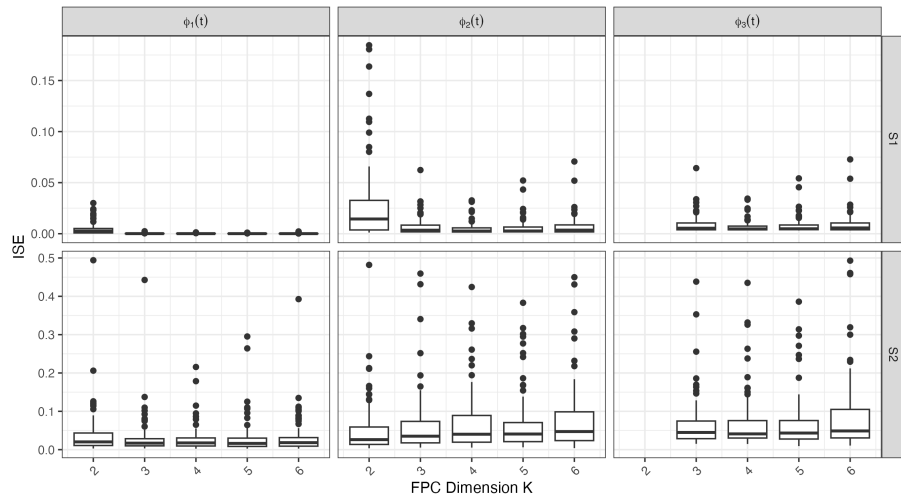


Figure S9: Boxplots of FPC ISE from applying FAST by number of chosen FPCs K . Columns indicate FPC, and rows correspond to simulation scenario.

Figure S9 indicates setting $K = 2$ produces biased estimates of $\phi_1(t), \phi_2(t)$ as expected, though it also shows that increasing $K \geq 3$ does not result in substantial bias estimating the first 3 FPCs.

Figure S10 similarly shows that $K = 2$ produces non-optimal inference for $\phi_1(t), \phi_2(t)$, with inferences for the first 3 FPCs unaffected when $K > 3$.

S4.2 Chosen spline dimension Q

We next vary the spline basis dimension Q used by FAST to estimate the functional components of FPCA. We vary between $Q = 5$ and $Q = 40$ to understand the effects of both

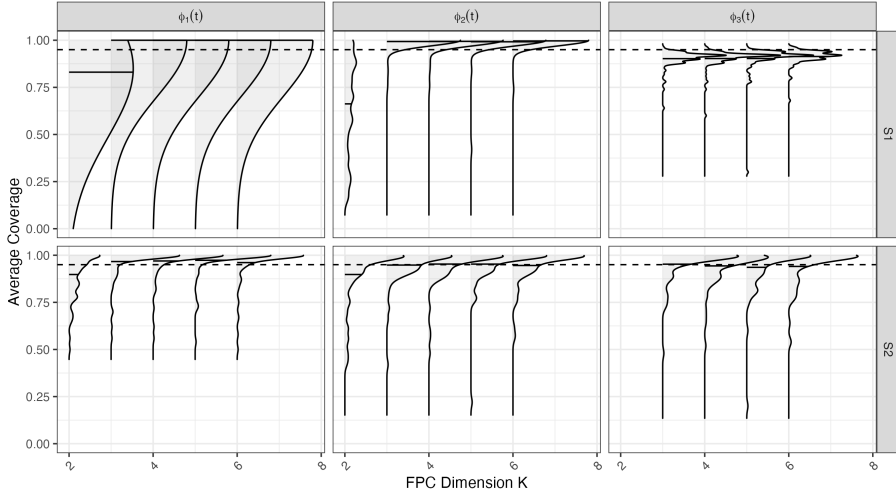


Figure S10: Kernel smooths of true FPC 95% credible interval coverage probabilities for FAST by number of chosen FPCs K . Columns indicate FPC, and rows correspond to simulation scenario.

having a rather restrictive basis as well as having one which is very rich. We evaluate FAST under each Q value using ISE and coverage of the FPCs as described in Section 4.

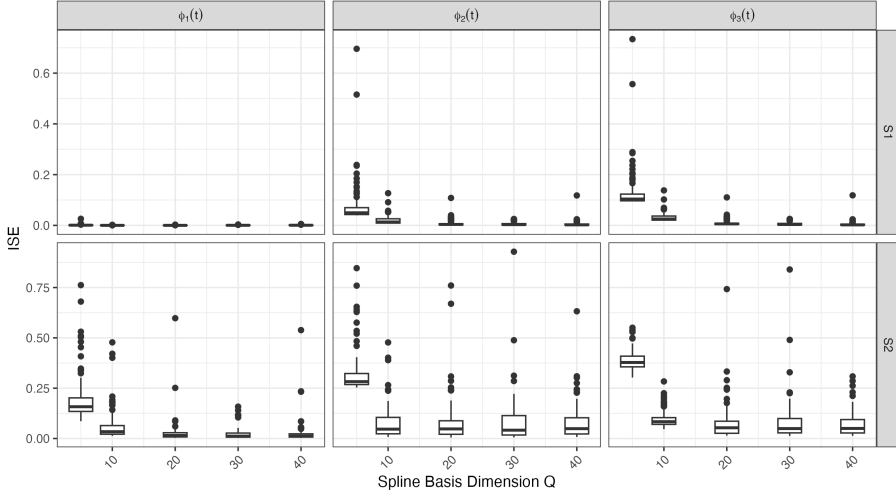


Figure S11: Boxplots of FPC ISE from applying FAST by spline basis dimension Q . Columns indicate FPC, and rows correspond to simulation scenario.

Figure S11 indicates setting $Q = 5$ produces biased estimates of the FPCs, likely due to lack of flexibility in the basis. However, the FPC ISE uniformly reduces and stabilizes by $Q = 20$ across both simulation scenarios.

Figure S12 similarly shows that $Q < 20$ produces non-optimal inference, with coverage stabilizing at near nominal levels for $Q \geq 20$.

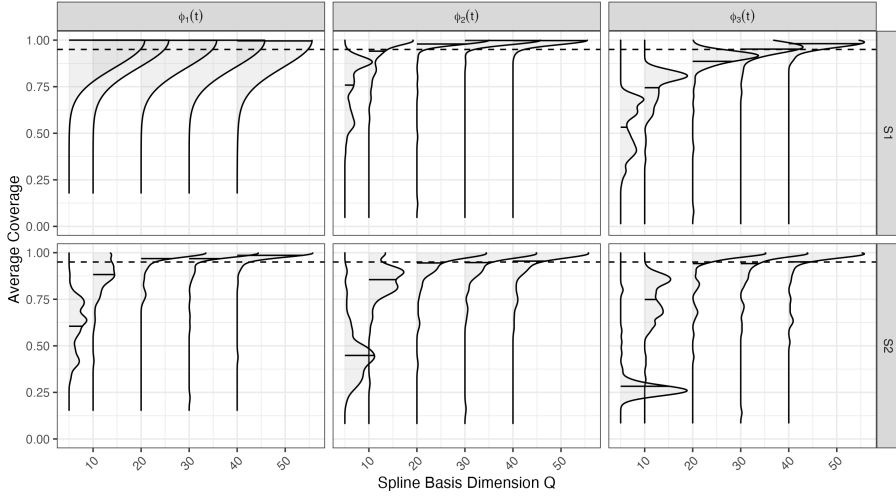


Figure S12: Kernel smooths of true FPC 95% credible interval coverage probabilities for FAST by spline basis dimension Q . Columns indicate FPC, and rows correspond to simulation scenario.

S4.3 Chosen penalty parameter α

We finally vary penalty hyperparameter α , which dictates the proportion of the smoothing penalty used by FAST which focuses on absolute value rather than second-order variation. We vary between $\alpha = 0.01$ and $\alpha = 0.3$, keeping $\alpha < 0.5$ to ensure the majority of the penalty is focused on the "wiggleness" which should be the core of any smoothing penalty. We evaluate FAST under each α value using ISE and coverage of the FPCs as described in Section 4.

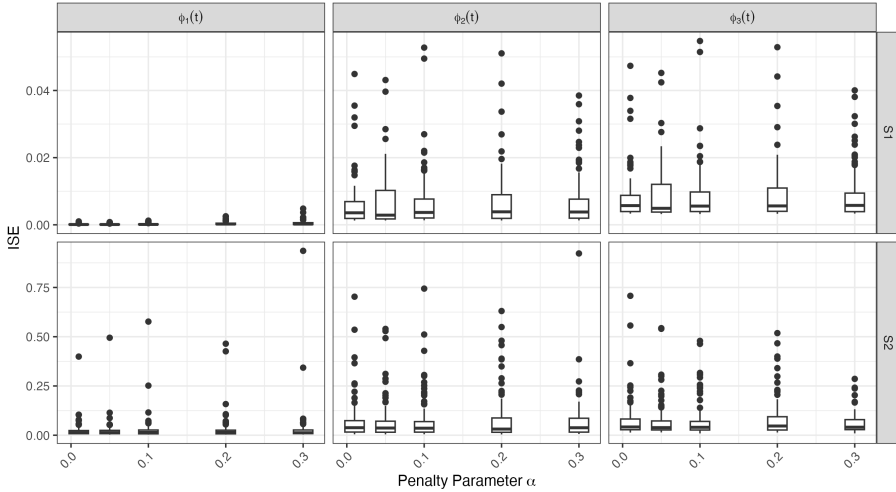


Figure S13: Boxplots of FPC ISE from applying FAST by penalty parameter α . Columns indicate FPC, and rows correspond to simulation scenario.

Figure S13 indicates that estimation accuracy, evaluated using ISE between the esti-

mated and true FPCs, is consistent across the range of α values tested.

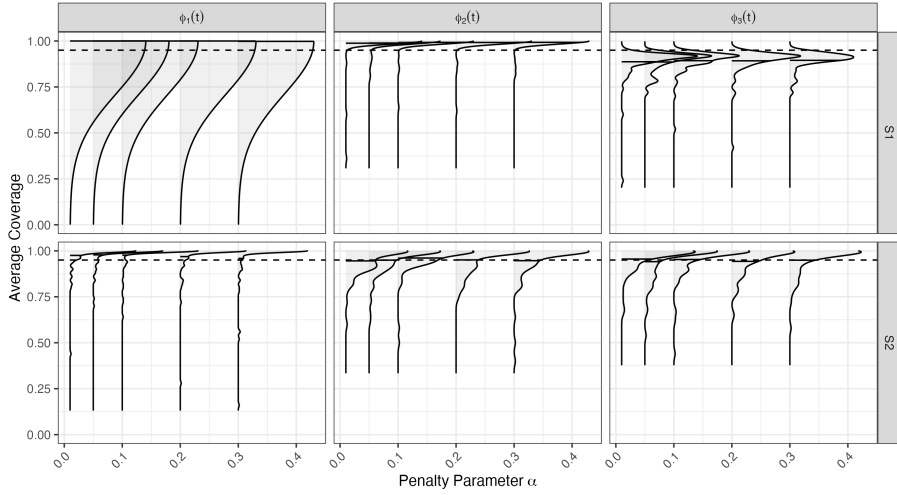


Figure S14: Kernel smooths of true FPC 95% credible interval coverage probabilities for FAST by penalty parameter α . Columns indicate FPC, and rows correspond to simulation scenario.

Figure S14 indicates that inference, evaluated using point-wise coverage of the true FPCs by equal-tailed 95% credible intervals, is also consistent across the range of α values tested.

S4.4 Timing by Q, K

Given that it appears that estimation accuracy and inference are consistent when K and Q are sufficiently large, we evaluate the effect of increasing these quantities on the computation time of FAST. For this experiment, we focus on S1, the more computationally complex simulation scenario based upon CGM data. For each combination of $K \in \{3, 4, 5\}$ and $Q \in \{20, 30, 40\}$, we timed FAST on the same personal laptop described in Section 4 (2023 MacBook Pro with Apple M2 Max@3.49 GHz and 32GB of memory).

K/Q	$Q = 20$	$Q = 30$	$Q = 40$
$K = 3$	3.5	3.9	3.6
$K = 4$	4.3	3.7	4.0
$K = 5$	5.4	4.6	5.7

Table S1: Table of FAST BayesFPCA computation times (in minutes) for each combination of spline dimension Q and number of FPCs K . We fix the simulation to S1, number of time series to $N = 50$, and number of observations along the domain to $M = 50$.

From Table S1, we find that FAST does require additional computation time when Q, K are increased, particular when K is made larger. However, the change in computation time

is relatively marginal, and FAST is still more efficient in every case than the comparator MCMC-based methods tested on the same problem in Table 1.

S5 Additional CGM Analyses/Details

S5.1 Variability explained - Single Level

We plot the variability explained versus the number of FPCs used, K , for each of the 4 sub-diets in Figure S15. These values are calculated using frequentist FACE estimates of FPCA for each K value.

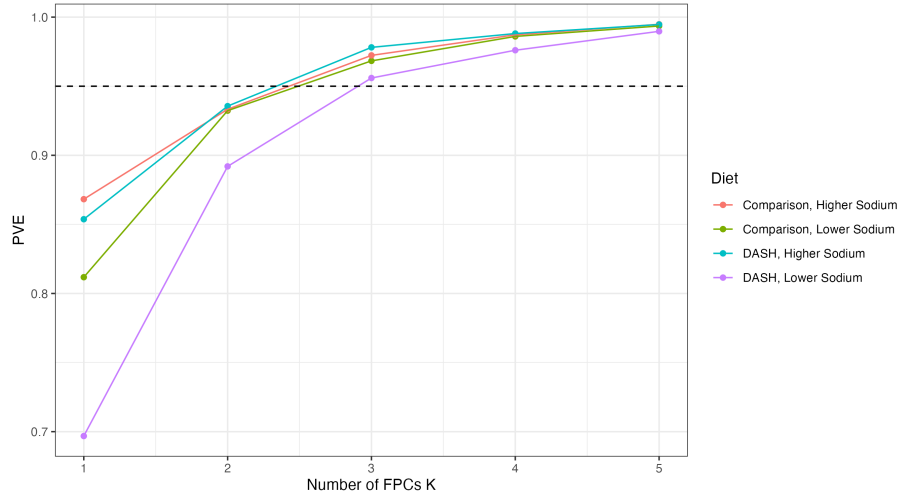


Figure S15: Variability in the single-level mean CGM curve data explained by FPCA approximation over a range of K values, stratified by diet.

Figure S15 indicates that, for all diets, $K = 3$ principal components explains more than 95% of the variability.

S5.2 Bayesian FPCA of randomly-chosen CGM within diets

As an alternative single-level analysis, we randomly sample a function for each participant within each diet rather than aggregating. These functions each represent a single instantiation of the meal process for that participant within the particular diet, whereas the aggregate functions analyzed in Section 5.2 have varying levels of noise based upon the number of curves included in the average. However, when performing the by-diet FPCA analyses on these randomly chosen curves instead of the aggregated CGM, we observe qualitatively identical results. We first present the eigenfunctions with associated uncertainty in Figure S16. The primary difference we observe is in the additional sampling variability of $\hat{\phi}_1(t)$ for the DASH, Lower Sodium diet, along with some of the posterior samples having

greater curvature. This is indicative of differences in mean mealtime glucose being much lower for this population, reduced to be on similar scale to differences peakedness.

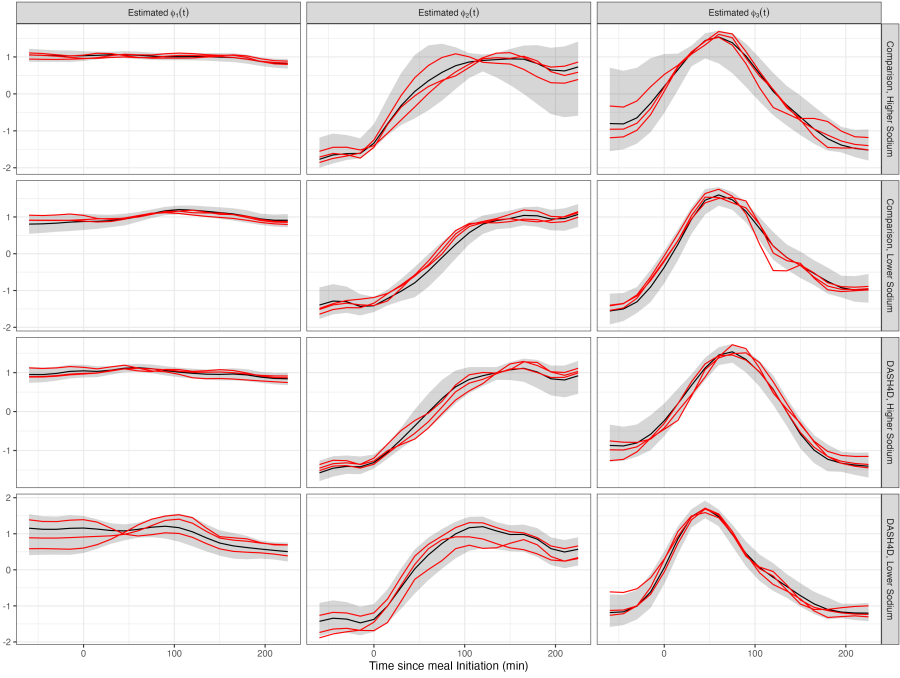


Figure S16: Bayesian FPCA results for the first three PCs (each column corresponds to one FPC) for each of the four diets (each row corresponds to one diet). X-axis: time from the start of the meal. Black curves: posterior mean; red curves: three samples from the posterior of the PCs; shaded areas: pointwise 95% credible intervals.

We present also the corresponding eigenvalues in Figure S17, where again one observes the unique properties of the DASH, Lower Sodium diet. In this analysis as well, there is lower overall variability for this diet (assessed by sum of eigenvalues). This difference is again driven by the first eigenvalue/eigenfunction pair in this analysis.

As for the aggregate data, we fit each model using 5000 iterations with the first 2500 discarded as burn-in. Employing the routine from Section 2.5 to assess convergence of the scores and FPCs, we found final Gelman-Rubin statistics were ≤ 1.02 .

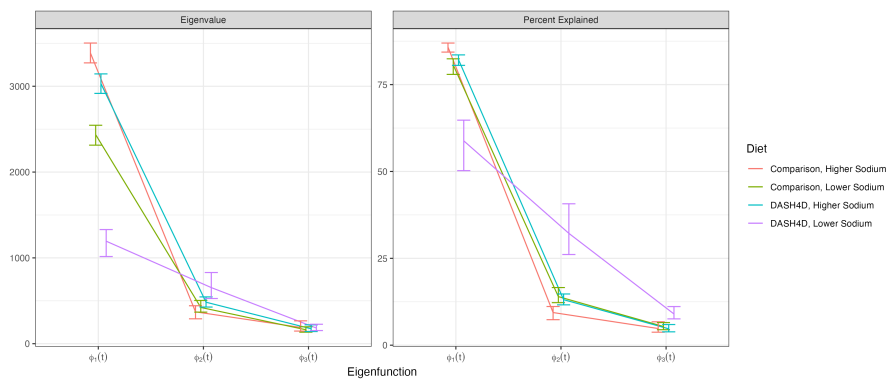


Figure S17: Eigenvalue and percent-variability estimates from the Bayesian FPCA models fit to each of the four diets (each line and color corresponds to one diet). X-axis: eigenfunction corresponding to eigenvalue/percent variance explained. All estimates are presented with their corresponding 95% credible intervals.